TU Delft

Delft University of Technology

Document Version
Final published version

Licence
CC BY

Citation (APA)
Engelhardt, F., Bondarenko, A. V., Metelmann, A., Blanter, Y. M., Viola Kusminskiy, S., & Bittencourt, V. A. S. V. (2026). Optics-microwave entanglement and state teleportation mediated by a cavity magnomechanical system. *Quantum Science and Technology*, *11*(4), Article 0450c8. https://doi.org/10.1088/2058-9565/aebe62

Important note
To cite this publication, please use the final published version (if applicable).
Please check the document version above.

Copyright
In case the licence states “Dutch Copyright Act (Article 25fa)”, this publication was made available Green Open Access via the TU Delft Institutional Repository pursuant to Dutch Copyright Act (Article 25fa, the Taverne amendment). This provision does not affect copyright ownership.
Unless copyright is transferred by contract or statute, it remains with the copyright holder.

Sharing and reuse
Other than for strictly personal use, it is not permitted to download, forward or distribute the text or part of it, without the consent of the author(s) and/or copyright holder(s), unless the work is under an open content license such as Creative Commons.

Takedown policy
Please contact us and provide details if you believe this document breaches copyrights.
We will remove access to the work immediately and investigate your claim.

This work is downloaded from Delft University of Technology.

Quantum Science and Technology

Celebrating the 10th anniversary of Quantum Science and Technology
PURPOSE-LED PUBLISHING™

PAPER • **OPEN ACCESS**

Optics-microwave entanglement and state teleportation mediated by a cavity magnomechanical system

To cite this article: F Engelhardt *et al* 2026 *Quantum Sci. Technol.* **11** 0450c8

View the article online for updates and enhancements.

You may also like

- Quantum circuits for high-dimensional absolutely maximally entangled states
Berta Casas, Grzegorz Rajchel-Mieldzio, Suhail Ahmad Rather et al.
- Roadmap on quantum thermodynamics
Steve Campbell, Irene D'Amico, Mario A Ciampini et al.
- Iterative optimization in quantum metrology and entanglement theory using semidefinite programming
Árpád Lukács, Róbert Trényi, Tamás Vértesi et al.

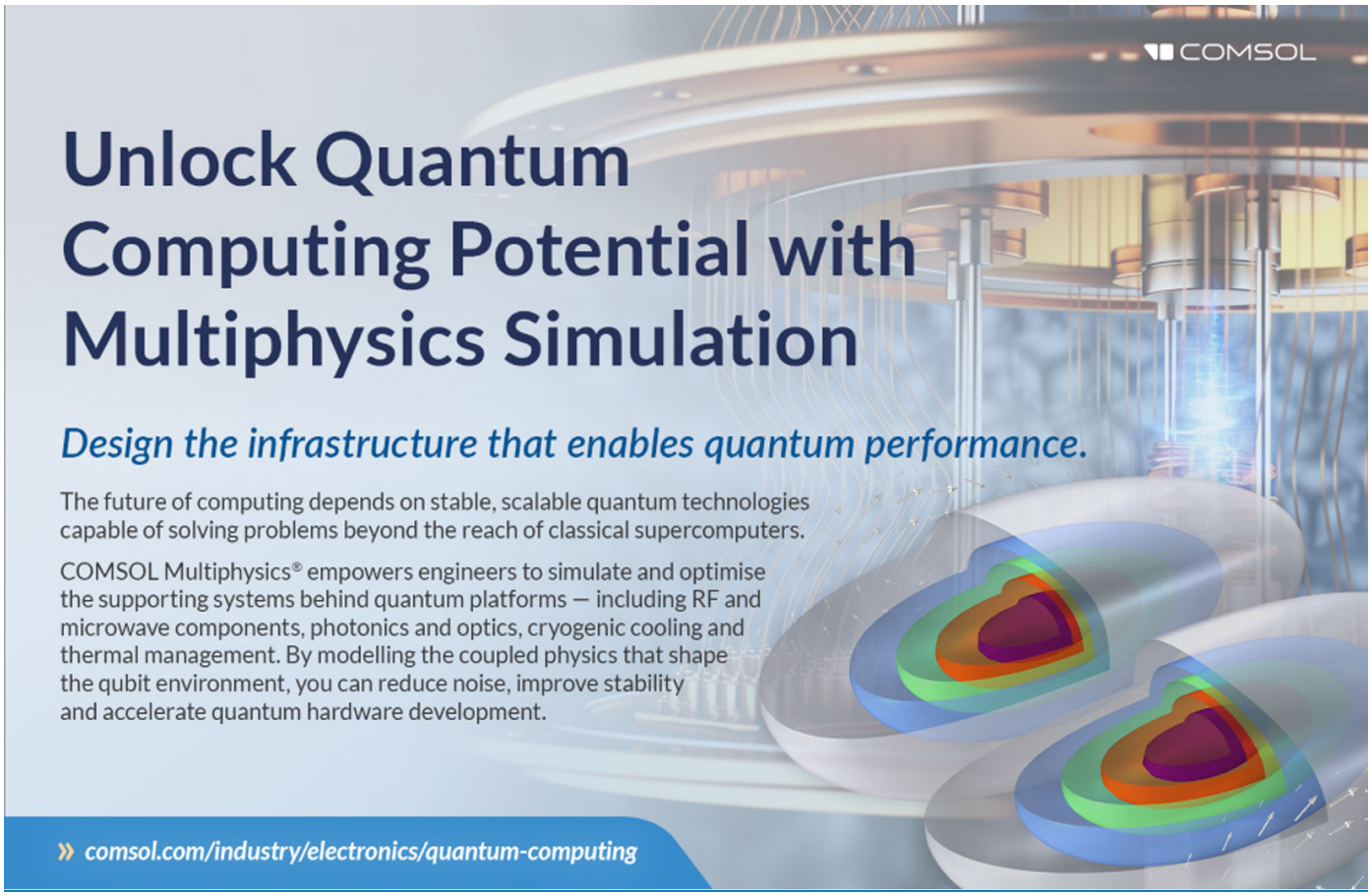

This content was downloaded from IP address 145.90.36.48 on 23/11/2026 at 14:29

Quantum Science and Technology

Check for updates

OPEN ACCESS

RECEIVED
17 June 2026

REVISED
22 October 2026

ACCEPTED FOR PUBLICATION
5 November 2026

PUBLISHED
17 November 2026

Original content from this work may be used under the terms of the Creative Commons Attribution 4.0 licence.

Any further distribution of this work must maintain attribution to the author(s) and the title of the work, journal citation and DOI.

PAPER

Optics-microwave entanglement and state teleportation mediated by a cavity magnomechanical system

F Engelhardt[1,2], **A V Bondarenko**[3,4], **A Metelmann**[5,6], **Ya. M Blanter**[3], **S Viola Kusminskiy**[1,2,*] and **V A S V Bittencourt**[7]

[1] Institute for Theoretical Solid State Physics, RWTH Aachen University, 52074 Aachen, Germany
[2] Max Planck Institute for the Science of Light, Staudtstr. 2, PLZ 91058 Erlangen, Germany
[3] Kavli Institute of Nanoscience, Delft University of Technology, Delft 2628CJ, The Netherlands
[4] Institute of Magnetism of NAS and MOS of Ukraine, Kyiv 03142, Ukraine
[5] Institute for Theory of Condensed Matter and Institute for Quantum Materials and Technology, Karlsruhe Institute of Technology, 76131 Karlsruhe, Germany
[6] ISIS (UMR 7006), Université de Strasbourg, 67000 Strasbourg, France
[7] Instituto de Física, Universidad Nacional Autónoma de México, 04510 Mexico City, Mexico
[*] Author to whom any correspondence should be addressed.

E-mail: kusminskiy@physik.rwth-aachen.de and engelhardt@physik.rwth-aachen.de

Keywords: magnomechanics, continuous variable entanglement, quantum physics, state teleportation

Abstract

Generating usable output-entanglement in continuous variable systems can serve as a viable resource for improving applications in quantum information science. In this work, we show how to generate steady-state output-entanglement in a two-stage conversion setup between optical and microwave photon which employs resonantly coupled magnetic and mechanical excitations, as proposed in (2022 *Phys. Rev. Appl.* **18** 044059). We show that the entanglement can be maximized for the same set of parameters which optimize the frequency-conversion efficiency, and that it can be leveraged for a teleportation-based state-transfer protocol for coherent input-states with fidelity close to unity. We propose an implementation based on an yttrium iron garnet disk of micrometer scale, and use both simulation results and reasonable estimates to assess the performance under optimized conditions. We find a maximum teleportation fidelity of 0.75 for the proposed setup.

1. Introduction

Quantum entanglement is central to applications in quantum technologies, including cryptography [1–5], teleportation [6–13], sensing, and quantum networks [14–23]. Generating entanglement is, nevertheless, not a trivial task, in particular when the entangled degrees-of-freedom belong to systems operating at different frequencies, as it is the case for optical and microwave photons. While microwave photons can couple resonantly to superconducting qubits, a lead architecture for quantum computation [24], optical photons operate at much higher frequency and are ideal for transporting quantum information over long distances at low losses [25]. Entangling optical and microwave photons can thus enhance capabilities of quantum networks for information transfer and processing [26].

This can be achieved, for example, via direct electro-optic interaction [27–30], which was used in a recent seminal experimental demonstration [31]. Alternatively, one can use a mediator capable of coupling to both types of excitations, lifting some limitations. A prominent example are mechanical degrees of freedom, which can mediate engineered interactions between itinerant and output modes [32–44]. Efficient coupling to photons can be achieved by hosting microwave-frequency phonons in an optical and microwave cavity, which enhances the coupling strength due to the confinement of photons. The radiation-pressure interaction between optical photons and phonons allows the activation of a photon-phonon pair creation process via an optical drive set at a frequency higher from the cavity by one phonon frequency (blue detuning). The same driving scheme can, in principle, also be applied to a system that uses magnetic degrees of freedom as mediator via magneto-optical interactions [45]. In contrast to phonons, whose frequencies are generally fixed by the resonator design, the magnetic excitations

© 2026 The Author(s). Published by IOP Publishing Ltd

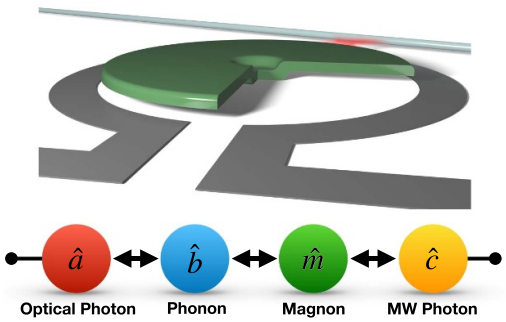

Figure 1. 3D render of the proposed geometry. A telecom-frequency light field inside an optical fiber couples evanescently to a micromagnetic disk. The disk serves as optical cavity while simultaneously hosting mechanical and magnetic modes as well. The last element is a dark-gray omega-shaped microwave ring resonator. In our simulations, the disk has radius 3.7 μm and thickness 200 n m. The envisioned coupling scheme is pictured below the setup.

(magnons) are easily tunable via an external magnetic field, which adds flexibility in design and makes them a promising new candidate for applications in quantum information processing [46–55].

The capacity of a setup based on hybrid quantum systems to generate and distribute entanglement is generally dependent on how strong the subsystems interact. Together with taking into account their individual lifetimes, this can be quantified by the cooperativity. For two systems A and B, the cooperativity is defined as $C_{AB} = 4g_{AB}^2/\kappa_{A,\mathrm{tot}}\kappa_{B,\mathrm{tot}}$, where g_{AB} is the coupling strength and $\kappa_{A/B,\mathrm{tot}}$ the respective total linewidth. A setup with one mediator between two output modes is thereby quantified by two cooperativities. It has been shown that for one-stage setups maximum output entanglement occurs for matching cooperativities [56]. This condition is one of the main bottlenecks for one-stage setups, therefore devices bridging optics and microwaves would benefit from added tunability, which further gives rise to more flexibility in design and functionality. This can be achieved by combining magnons and phonons and using their strong resonant interaction [57, 58] as mediator. In essence, the magnomechanical interaction can be used as a two-stage mediator for optics-to-microwave frequency conversion, in which cooperativity constraints typically encountered on single-stage converters are lifted [59]. Experimental platforms based on magnomechanics have advanced rapidly in recent years, with progress especially driven by advances in device fabrication at the microscale [57, 58, 60–63]. While adding an extra degree of freedom increases the complexity of the system, it also relaxes design constraints. As in one-stage platforms, in magnomechanical devices optimizing all the coupling rates is challenging. However, as it was shown in [59] for frequency transduction, and as we show here for entanglement generation, this condition is not necessary for two-stage devices, where there is a large regime of parameters for which optimal functionality can be achieved. This tunability together with the recent experimental advances justify proposing and benchmarking quantum protocols for realistic magnomechanical platforms, including the device geometry.

In this work, we investigate the optimal conditions for generating entanglement between an output optical mode and an output microwave mode which interact via a hybrid magnomechanical system shown in figure 1: a magnetic dielectric that simultaneously serves as an optical cavity while also hosting the mechanical mode, and is coupled to a microwave resonator. The optical and microwave modes further couple to external ports, which can be, for example, an optical fiber and a microwave cable, respectively. The optical mode is driven with a blue-detuned coherent drive, which generates entanglement between optical photons and phonons. The interaction between phonons and magnons, and between magnons and microwaves, distributes the correlation among the constituents of the systems, ultimately entangling the optics and microwave outputs. Remarkably, obtaining maximum output entanglement does not require matching cooperativities, which is similar to what we obtained previously for frequency conversion [59] in the same two-stage setup, however with stricter limitations imposed by temperature and port-coupling efficiencies.

We benchmark the entanglement capacity on the continuous variable teleportation scheme by Vaidman, Braunstein and Kimble (VBK) [9, 10]: the state to be teleported is mixed with one of the parts (which we label ‘a’ and represents the output optical mode) of an entangled bipartite state. The result is homodyne measured, and the outcome is used to displace the other part of the bipartite state (which we label ‘c’ and represents the output microwave mode). In the optimal case, the state of ‘c’ reproduces fully the state to be teleported. The performance of this protocol depends only on the generated steady-state entanglement [64] and does not require a tailored sequence of time-dependent coupling rates for

performing state transfer. We first analyze the performance for an optimal, geometry-agnostic microscale system, in which the different coupling strengths are set to the maximum theoretical value allowed by the system parameters, together with dissipation values taken from the literature. This serves as a benchmark for our proposed device setup (see figure 1), consisting of a magnetic microdisk resonator coupled to a microwave resonator and an optical fiber. The fabrication of magnetic microdisk devices has quickly developed in the last years [65–70], highlighting the potential of such a geometry for engineering hybrid devices. Our material of choice throughout the manuscript is yttrium iron garnet (YIG), a staple choice in magnonics experiments that provides long lifetime of magnon excitations and large spin density [71–74]. Alternative materials are mentioned in the outlook. Using simulation results for our proposed device and experimentally feasible estimates we predict a maximum teleportation fidelity of about 0.75 for this particular setup. Our results provide a realistic benchmark for harnessing entanglement in hybrid magnomechanical systems, yielding useful design guidelines and assessing unexplored capabilities of such devices for quantum technologies.

The manuscript is structured as follows. In section 2 we introduce the model for the optomagnomechanical system [59] and outline the blue-detuned optical driving scheme. Relevant parameters for an idealized system, in which all modes are assumed to perfectly overlap, are summarized in table 1. In section 3 we quantify the entanglement between the output microwave and optical modes using the logarithmic negativity [75]. Afterwards in section 4 we introduce the VBK continuous variable teleportation scheme [9, 10], and quantify the expected fidelity for coherent and squeezed states. We discuss imperfections that might reduce the fidelity in form of temperature and internal versus external dissipation. In section 5, we propose and benchmark the state-transfer protocol on a setup where the magnomechanical element is a YIG microdisc. The relevant parameters, such as coupling and decay rates, are obtained via simulations considering the proposed geometry. Conclusions and a brief outlook are presented in section 6. Details of the calculations together with extended analysis are presented in the Appendices.

2. Model

We consider a device fabricated of a magnetic material (compare figure 1) in which an optical mode $\hat{a}$, an elastic mode $\hat{b}$, a magnon mode $\hat{m}$ and a microwave mode $\hat{c}$ are co-localized. We consider modes $\hat{b}$, $\hat{m}$ and $\hat{c}$ to be close in frequency, while the optical mode $\hat{a}$ exhibits a higher frequency. In our envisioned device, the modes are coupled in the chain-like configuration shown in figure 2. Photons of mode $\hat{a}$ interact with the phonons of mode $\hat{b}$ via radiation-pressure: the elastic vibrations modulate the frequency of the optical mode [76]. Phonons couple via the magnetoelastic interaction [77, 78] to magnons in mode $\hat{m}$ and, in contrast to existing works [79, 80], we work with a resonant interaction between magnons and phonons. Finally, microwave modes $\hat{c}$ couple via the standard magnetic-dipole interaction to magnons [81, 82]. A more detailed modeling of each of those interactions and the corresponding coupling rates can be found in [59]. Typically, the optomagnonic and electromechanical couplings can be neglected in comparison with the other coupling rates. The dynamics of the different modes of such a device is modeled by the bosonic Hamiltonian

$$\begin{aligned}\frac{\hat{H}}{\hbar} &= \omega_a \hat{a}^\dagger \hat{a} + \omega_m \hat{m}^\dagger \hat{m} + \omega_b \hat{b}^\dagger \hat{b} + \omega_c \hat{c}^\dagger \hat{c} \\ &\quad + g_{ab} \hat{a}^\dagger \hat{a} \left(\hat{b}^\dagger + \hat{b}\right) + g_{mb} \left(\hat{b}^\dagger + \hat{b}\right) \left(\hat{m}^\dagger + \hat{m}\right) \\ &\quad + g_{mc} \left(\hat{m}^\dagger + \hat{m}\right) \left(\hat{c}^\dagger + \hat{c}\right) + \hat{H}_{\mathrm{Drive}}/\hbar ,\end{aligned} \tag{1}$$

where $\hat{H}_{\mathrm{Drive}} = i\xi \left(\hat{a} e^{i\omega_D t} - \hat{a}^\dagger e^{-i\omega_D t}\right)$ is a coherent drive of the optical mode with amplitude ξ. Under a strong drive, we can focus on the dynamics of the weak fluctuations $\hat{a} = \alpha + \delta\hat{a}$, where α is a coherent amplitude of the optical mode. Keeping only second order terms in the fluctuations $\delta\hat{a}$ yields the quadratic Hamiltonian (written in a frame rotating with $\omega_D \hat{a}^\dagger \hat{a}$)

$$\begin{aligned}\frac{\hat{H}}{\hbar} &= -\Delta \delta\hat{a}^\dagger \delta\hat{a} + \omega_m \hat{m}^\dagger \hat{m} + \omega_b \hat{b}^\dagger \hat{b} + \omega_c \hat{c}^\dagger \hat{c} \\ &\quad + G \left(\delta\hat{a}^\dagger + \delta\hat{a}\right) \left(\hat{b}^\dagger + \hat{b}\right) + g_{mb} \left(\hat{m}^\dagger \hat{b} + \hat{m} \hat{b}^\dagger\right) \\ &\quad + g_{mc} \left(\hat{m}^\dagger \hat{c} + \hat{m} \hat{c}^\dagger\right) ,\end{aligned} \tag{2}$$

Table 1. Values for mode frequencies, linewidths/dissipations and coupling strengths taken from [59].

Quantity	Symbol	Value
Optical photon freq.	$\omega_a/2\pi$	200 THz
Optical detuning (blue)	$\Delta_a/2\pi$	10 GHz
Phonon freq.	$\omega_b/2\pi$	10 GHz
Magnon freq.	$\omega_m/2\pi$	10 GHz
Internal optical linewidth	$\gamma_a/2\pi$	0.1 GHz
External optical dissipation	$\kappa_{a,\mathrm{out}}/2\pi$	1 GHz
Phonon linewidth	$\gamma_b/2\pi$	1 kHz
Magnon linewidth	$\gamma_m/2\pi$	1 MHz
Internal mw cavity loss rate	$\gamma_c/2\pi$	1 MHz
External mw cavity coupling rate	$\kappa_{c,\mathrm{out}}/2\pi$	100 MHz
Magnomechanical coupling	$g_{mb}/2\pi$	10 MHz
Magnon-Microwave photon coupling	$g_{mc}/2\pi$	180 MHz
Optomechanical coupling	$g_{ab}/2\pi$	0.2 MHz

where the detuning is given by $\Delta = \omega_D - \omega_a$. Due to the spatial confinement of the optical photons, the optomechanical coupling $G = \alpha g_{ab}$ scales with the square-root of the steady-state coherent number of photons inside the cavity $\alpha = \sqrt{\bar{n}_a}$ (see appendix A equation (A1)). We applied a rotating wave approximation, neglecting the terms proportional to $\hat{b}^\dagger \hat{m}^\dagger$ and $\hat{m}^{(\dagger)}\hat{c}^{(\dagger)}$. Also from now on, we adopt the notation $\delta\hat{a} \to \hat{a}$. In what follows, we consider numerical parameters summarized in table 1. Those are the same parameters used to evaluate microwave to optics transduction in [59], and they correspond to an idealized system in which the optomechanical and magnomechanical couplings assume perfect mode overlap, yielding their theoretical maximum. The linewidths of each mode are taken from different experimental references, and represent the typical values in such type of devices. See for example [83] for typical linewiths of the magnon and microwave modes, and [84] for optical and mechanical modes. This will be used as a base-line comparison between both applications. In section 5, we propose a physical system consisting of a magnetic disk coupled to a planar resonator as a promising platform to approach the ideal setup, and assess its performance for a state transfer scheme. The parameters for such an architecture are given in table 2.

In the quadratic Hamiltonian of equation (2), modes $\hat{b}$, $\hat{c}$ and $\hat{m}$ are close in resonance and can, depending on the coupling rates, form hybrid modes $\hat{d}_i$ with frequencies ω_i (with $i = 1,2,3$). The optical detuning Δ can then be used to activate different interactions between optical photons and the hybrid modes. Taking the parameters summarized in table 1, $g_{mc} \gg g_{mb}$, so that the hybrid modes are given by $\hat{d}_{1/2} = 1/\sqrt{2}\,(\hat{m} \pm \hat{c})$ at $\omega_{1/2} = \omega_{m/c} \pm g_{mc}$ and $\hat{d}_3 = \hat{b}$ at ω_b. For a red detuning $\Delta \approx -\omega_b$, meaning that one drives at a frequency that is lower than the cavity resonance frequency by ω_b, the relevant resonance is a beam-splitter interaction $\hat{a}^\dagger \hat{d}_i + h.c.$, which allows energy exchange between optics and the other modes by combining phonons and optical drive photons into resonant cavity photons. This is the basis for optics-to-microwave frequency conversion proposed in [59]. Here, we instead focus on the blue optical detuning case, $\Delta \approx \omega_b$, for which the relevant resonance is pair-creation and annihilation $\hat{a}^\dagger \hat{d}_i^\dagger + h.c.$, since the drive frequency is now larger than the cavity resonance frequency by ω_b. This interaction induces two-mode squeezing, which generates entanglement [85]. Our proposal harnesses such a correlation to entangle the output of the optical and the microwave modes, which can then propagate to other systems and be used as a resource for quantum information protocols, such as state transfer. Quantifying the capacity of our system for generating entanglement requires solving for the dynamics of the coupled equations of motions describing each mode.

We describe the open dynamics of the system via the Heisenberg–Langevin equations for each mode $\hat{o} = \hat{a}, \hat{b}, \hat{m}, \hat{c}$

$$\dot{\hat{o}} = -\frac{\mathrm{i}}{\hbar}\left[\hat{o}, \hat{H}\right] - \frac{\kappa_{\mathrm{o,\,tot}}}{2}\hat{o} - \sqrt{\kappa_{\mathrm{o,\,out}}}\,\hat{o}_{\mathrm{in,\,ext}} - \sqrt{\gamma_o}\,\hat{o}_{\mathrm{in,\,int}}\,, \tag{3}$$

where $\kappa_{\mathrm{o,\,tot}} = \gamma_{\mathrm{o}} + \kappa_{\mathrm{o,\,out}}$ is the total decay rate of mode $\hat{o}$, composed of an intrinsic contribution γ_{o} (e.g. optical absorption for the optical mode) and a contribution due to coupling to any output port $\kappa_{\mathrm{o,\,out}}$. The noise operators $\hat{o}_{\mathrm{in,\,int}}$ and $\hat{o}_{\mathrm{in,\,ext}}$ include both intrinsic noise and input contributions, and are assumed to be include thermal and vacuum fluctuations, given by

$$\begin{aligned}\left\langle \hat{o}_{\mathrm{in}}(t)\,\hat{o}_{\mathrm{in}}^\dagger(t')\right\rangle &= (n_{\mathrm{th,o}} + 1)\,\delta(t - t')\,,\\ \left\langle \hat{o}_{\mathrm{in}}^\dagger(t)\,\hat{o}_{\mathrm{in}}(t')\right\rangle &= n_{\mathrm{th,o}}\delta(t - t')\,.\end{aligned} \tag{4}$$

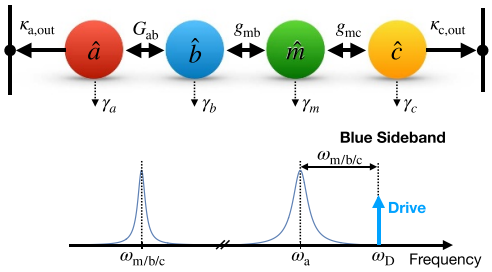

Figure 2. Schematic of the coupled system under consideration. As in the Hamiltonian equation (2), we denote optical photons as $\hat{a}$, phonons as $\hat{b}$, magnons as $\hat{m}$, and microwave photons $\hat{c}$. All modes have internal dissipation rates $\gamma_{a,b,m,c}$, and optical and microwave modes are additionally coupled to output ports with rates $\kappa_{a/c}$, out. Below the coupling scheme we show the considered driving scheme. The optical drive is placed at the blue sideband of the optical mode.

The Heisenberg–Langevin equations (See appendix A equations (A2*a*)–(A2*d*) for the explicit form) can be put in convenient matrix form

$$\dot{\hat{\mathbf{A}}} = \mathbb{A}\hat{\mathbf{A}} + \mathbb{B}\hat{\mathbf{A}}_{\text{in}}\,, \tag{5}$$

where the vector $\hat{\mathbf{A}}$ contains all creation and annihilation operators, and $\hat{\mathbf{A}}_{\text{in}}$ all the noise operators. Furthermore, the matrix $\mathbb{A}$ contains the elements of the equations of motion and matrix $\mathbb{B}$ the external and internal dissipation rates. More details can be found in appendix A.

3. Output entanglement

As outlined in the previous section, the two-mode squeezing interaction that is activated when the optical mode is driven at blue-detuning generates entangled pairs of excitations. Combined with beam-splitter interactions between the phonons, magnons and microwave photons (in the form of figure 2) the entanglement is distributed among all the constituents of the setup and eventually generates an entangled multipartite steady-state. In particular, the optical and microwave modes can become entangled, which we refer to intra-cavity entanglement. The modes $\hat{a}$ and $\hat{c}$ couple to output ports, and thus the output modes, obtained via the standard input-output relation (for $\hat{o} = \hat{a}, \hat{c}$)

$$\hat{o}_{\text{out}} = \hat{o}_{\text{in}} + \sqrt{\kappa_{o,\text{out}}}\hat{o}\,, \tag{6}$$

also get entangled. Here we are interested in the entanglement between the output modes, since they are the ones accessible experimentally and they can be used for performing state teleportation between optical and microwave photons. In this case, a state encoded in the input of the optics (microwave) mode is fully teleported to the output of the microwave (optics) mode, which can then propagate to other devices.

3.1. Covariance matrix and the negativity

Since the dynamics of the system, described by the Heisenberg–Langevin equations equation (5), are linear and we assume initial states of the modes to be vacuum, the steady-state of the system is Gaussian. Therefore, the state is fully characterized by its covariance matrix, containing the first and second moments of the modes' quadratures. We define

$$\hat{\mathbf{R}} = (\hat{x}_a, \hat{p}_a, \hat{x}_b, \hat{p}_b, \hat{x}_m, \hat{p}_m, \hat{x}_c, \hat{p}_c)\,, \tag{7}$$

where, e.g. $\hat{x}_a = \hat{a}^\dagger + \hat{a}$ and $\hat{p}_a = i\left(\hat{a}^\dagger - \hat{a}\right)$. The components of the covariance matrix are then given in terms of the correlations of the elements of $\hat{\mathbf{R}}$ defined by

$$\sigma_{ij} = \frac{1}{2}\langle \hat{R}_i\hat{R}_j + \hat{R}_j\hat{R}_i\rangle - \langle \hat{R}_i\rangle\langle \hat{R}_j\rangle\,. \tag{8}$$

The state of two selected subsystems, e.g. optical ($\hat{a}$) and microwave photons ($\hat{c}$), can be obtained by discarding the columns and rows of σ corresponding to the traced-out modes ($\hat{b}$ and $\hat{m}$).

With the covariance matrix describing the joint optics-microwave state, we can compute entanglement with the logarithmic negativity. Such a quantifier is based on the Simon-Duan criterion [86,

87]: the smallest symplectic eigenvalue of the partially transposed covariance matrix, which we indicate by η_-, is bounded from below for separable states. Hence, for entangled states, how much below this bound η_- lies can be used to quantify 'how far' a quantum state is from being separable. This is the continuous variable version of the positive-partial-transpose or Peres–Horodecki criterion [88, 89]. Given the covariance matrix between two modes i and j in the form:

$$\sigma_{ij} = \begin{pmatrix} B & C \\ C^T & B' \end{pmatrix}, \tag{9}$$

one can define the logarithmic negativity E_N [90] as

$$E_N = \max\left[0, -\ln\left(\eta_-\right)\right], \tag{10}$$

where η_- is given by

$$\eta_- = \frac{1}{\sqrt{2}}\sqrt{\Sigma - \sqrt{\Sigma^2 - 4\,\mathrm{Det}\left(\sigma_{ij}\right)}}, \tag{11}$$

with $\Sigma = \mathrm{Det}B + \mathrm{Det}B' - 2\,\mathrm{Det}C$.

3.2. Output entanglement

The output covariance matrix of our system is given by (see appendix D for the full derivation)

$$\sigma^{\mathrm{output}}\left[\omega\right] = \frac{1}{2}\left(S_{\mathbf{R}}\left[\omega\right] N_{\mathbf{R}} S_{\mathbf{R}}^T\left[-\omega\right] + S_{\mathbf{R}}\left[-\omega\right] N_{\mathbf{R}}^T S_{\mathbf{R}}^T\left[\omega\right]\right), \tag{12}$$

where $S_{\mathbf{R}}$ is the scattering matrix and $N_{\mathbf{R}}$ contains the quadrature noise elements. To assess the entanglement between optical and microwave outputs, we have to introduce filters at appropriate center-frequencies [31, 56]. For example, in the frame rotating at the cavity drive frequency, the optical mode is given via

$$\hat{A}_{\mathrm{out}}\left(\omega, \sigma\right) = \int_{-\infty}^{\infty} \mathrm{d}\omega' f(\omega - \omega', \sigma)\, \hat{a}_{\mathrm{out}}\left(\omega'\right), \tag{13}$$

where σ is the bandwidth of the applied filter function f. Filtering the output modes assures that only photons at appropriate frequencies are compared when quantifying the entanglement. The filter bandwidth must be considered because in reality one only has access to a finite time interval when taking measurements of a given mode, and therefore to a finite spectral interval. From now on we refer to ω as the filter center frequency, and consider exclusively the case of a narrow bandwidth filter. We quantify the effect of a finite filter bandwidth in appendix D. For the case that $\omega_m = \omega_b = \omega_c = \Delta_a$ and considering all modes are filtered according to equation (13) with center frequency $\omega = \Delta_a$, the output covariance matrix has the form

$$\sigma_{\mathrm{ac}}^{\mathrm{output}} = \begin{pmatrix} c_1 & 0 & 0 & c_3 \\ 0 & c_1 & c_3 & 0 \\ 0 & c_3 & c_2 & 0 \\ c_3 & 0 & 0 & c_2 \end{pmatrix}, \tag{14}$$

where $c_{1,2,3}$ are functions of the cooperativities $C_{ij} = 4g_{ij}^2/\kappa_{i,\mathrm{tot}}\kappa_{j,\mathrm{tot}}$. The exact functional forms are not illuminating and are provided in appendix D. The choice of the filter center frequency is pivotal, since it assures that modes are considered at appropriate frequencies in the entanglement quantification, namely an optical photon at ω_a and a microwave photon at ω_c. The logarithmic negativity is calculated using equation (10). In typical magnomechanical systems at the microscale, it is possible to bring selected magnon and phonon modes in resonance by tuning an external magnetic field, whereas the magnon-phonon coupling is fixed by the magnet's geometry which determines the allowed modes and their overlap. Thus, the main controllable parameters that define the steady-state of the outputs are the optomechanical and the magnon-microwave cooperativities, C_{ab} and C_{mc} respectively. The optomechanical cooperativity C_{ab} can be set by the input power applied to the optical mode, while C_{mc} can be changed by placement of the magnet in a microwave cavity (in the case of a 3D cavity), or by changing the relative position of the magnet with respect to a planar cavity.

In figure 3 we plot the logarithmic negativity E_{N} of the state shown in equation (14) as a function of the optomechanical and magnon-microwave cooperativity at fixed magnomechanical cooperativity. Using

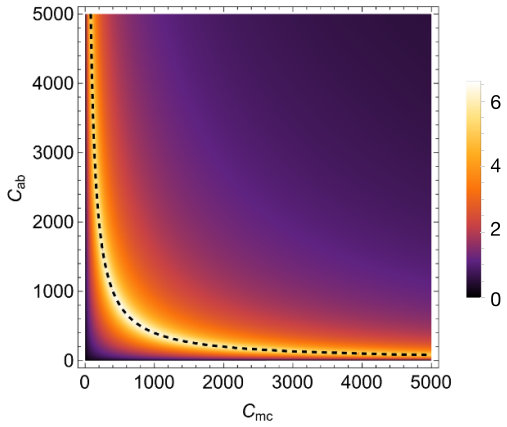

Figure 3. Logarithmic negativity E_N as function of optomechanical (C_{ab}) and magnon-microwave (C_{mc}) cooperativity. The magnomechanical cooperativity was set to $C_{mb} = 4 \times 10^5$ which is based on to the values in table 1 and ensures comparability with [59]. The black dashed line corresponds to setting the denominator equal to zero in equation (D8) of appendix D, given by the function $C_{ab} = 1 + {}^{C_{mb}}/_{(C_{mc}+1)}$, and corresponds to an unstable parameter regime.

the same parameters (see table 1), we notice an identical qualitative behavior as for the maximum conversion efficiency discussed in figure 3(a) of [59]. In particular, one does not require matching cooperativities to reach maximum E_N, as it would be the case for one-stage setups. Physically, this corresponds to a point where the system reaches a parametric instability. This is special for the case of blue optical detuning, since it drives a particle non-conserving process. So when the rate at which pairs of excitations are created is not compensated by the system's dissipation rates, the linear system never reaches a steady-state. For red optical detuning, as in the case for frequency conversion, only particle conserving processes are relevant, and the system is instead pushed close to a transition to different mode hybridization. This is illustrated in figure 4(a) by plotting E_N as a function of the magnon frequency and for different optomechanical coupling rates G, which define the strength of the pair-creation interaction and can be increased by the optical pump power. As G increases, so does E_N, while simultaneously the region of stability becomes more narrow. The largest G ($\alpha \approx 42$) puts the system in the maximum entanglement region, in agreement with figure 3. In figure 4(b) we reduce the magnon-microwave coupling rate by one order of magnitude, which results in a shift of the regions of largest entanglement generation in accordance with the change of hybridization in the system. Hybrid mode frequencies can be easily obtained by numerically calculating the eigenvalues of matrix $\mathbb{A}$ in equation (5) [59]. It is important to note that we have so far considered zero temperature, and no internal dissipation of the optical and microwave modes, hence the port coupling efficiencies are 1. Under these circumstances we can conclude that classical frequency conversion and quantum bipartite entanglement can be optimized for the same parameters. The effect of internal losses together with other imperfections will be discussed in section 4.2.

The interaction that generates entanglement produces pairs of excitations and, depending on the strength of the coupling rate and other relevant parameters, the system can become unstable. The stability of the system can be analyzed with the eigenvalues $\{\lambda_i\}$ of the dynamical matrix $\mathbb{A}$ in equation (5). If $\mathrm{Re}[\lambda_i] < 0$ for all the eigenvalues, the system is linearly stable. We then obtain the eigenvalues $\{\lambda_i\}$ numerically, and used them to delimit the stability regions in figure 4. We present in appendix B a more complete analysis, including stability diagrams as a function of the optical pump enhancement α and the magnon frequency ω_m.

Experimentally, the elements of the covariance matrix can be reconstructed via homodyne measurements. This is done by mixing each output with a strong local coherent signal in a 50:50 beam-splitter, and then measuring the photocurrent in one of the beam-splitter ports. The experimental signal consists of time-dependent optical and microwave heterodyne currents, which fluctuate in time and in each experimental run. Those signals can be used to calculate correlations in Fourier domain, which, when averaged over all experimental runs, can be directly related to antisymmetrized correlations [91], which are then used to reconstruct the covariance matrix. This is a standard procedure for measuring Gaussian correlations used in different state-of-the-art experiments, e.g. in [31]. Measurements via heterodyning are also possible, with the advantage of simpler setups but the drawback of more added noise [92].

Finally, we note that the optical mode can couple directly to the magnon mode via magneto-optical effects, provided that mode and symmetry matching conditions are fulfilled [93, 94]. We provide an

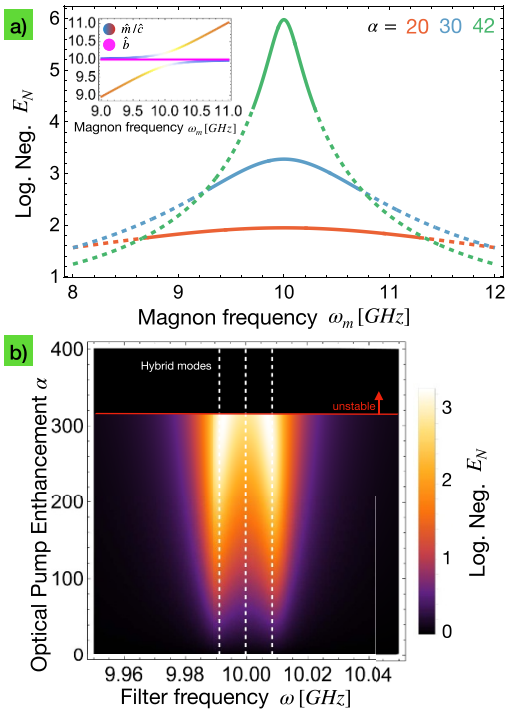

Figure 4. (a) Output entanglement quantified in terms of the logarithmic negativity as a function of the magnon frequency ω_m. We vary the optomechanical pump enhancement factor α, all other parameters are in accordance with table 1. Dotted lines indicate where the system becomes unstable. The inset shows the mode hybridization as a function magnon frequency for the phonon-magnon-microwaves subsystem. In plot (b), we reduce the magnon-microwave coupling to $g_{mc} = 18\,\mathrm{MHz}$, and plot the logarithmic negativity both as a function of the filter center frequency ω, and the enhancement factor α. The reduced coupling leads to a shift of the entanglement maxima in accordance with the changed hybrid mode frequencies, indicated by the white dashed vertical lines. The red horizontal line signifies the transition to the unstable regime.

analysis of the effects of such an optomagnonic coupling g_{am} in appendix C, where we show that such effects are only relevant if $g_{am} > g_{ab}$. While this is possible in some circumstances [95], for a system made with YIG under optimal mode-matching conditions [93, 96] we estimate that $g_{am} \sim g_{ab}$ (see appendix C). Even in this regime, the effects of the optomagnonic coupling for the microwave-optics entanglement can be disregarded.

4. Teleportation state-transfer

4.1. VBK setup

In this section we evaluate the performance of the system considering a particular task which harnesses output entanglement. Entanglement is a required resource to perform teleportation [97]. For continuous variable systems, the teleportation protocol proposed by VBK [9, 10] uses two-mode squeezed states, and displacements conditioned on homodyne measurements. The goal of the scheme is to transfer a continuous variable state from a party, which we label 'a', to another party, which we label 'c'. Party 'a' is assumed to share a two-mode squeezed state with 'c'. The state to be transferred is mixed via a 50:50 beam-splitter with 'a's part of the two-mode squeezed state. Balanced homodyne detection is performed, yielding the complex amplitude z. Such an amplitude determines a displacement $\hat{D}(z)$ to be applied to the 'c' part of the two-mode squeezed state. Such a protocol uses steady-state entanglement to improve the transfer fidelity for states of continuous variables [64]. In our setup, the output entanglement is generated by the two-mode squeezing operation provided by the blue-driven optomechanical interaction.

Therefore, the two-mode squeezed state of the original VBK setup is obtained as the entangled output from the hybrid chain as depicted in figure 5. At zero temperature, the performance of this protocol is only dependent on the amount of steady-state entanglement that can be generated between input and output. This is set by the system design and the optical drive, and therefore does not require the control of the intermediate coupling rates. Such a protocol is better suited to magnomechanical systems compared to state-transfer protocols that require temporal control of coupling strengths or to use dark modes to mitigate dissipation loss [98].

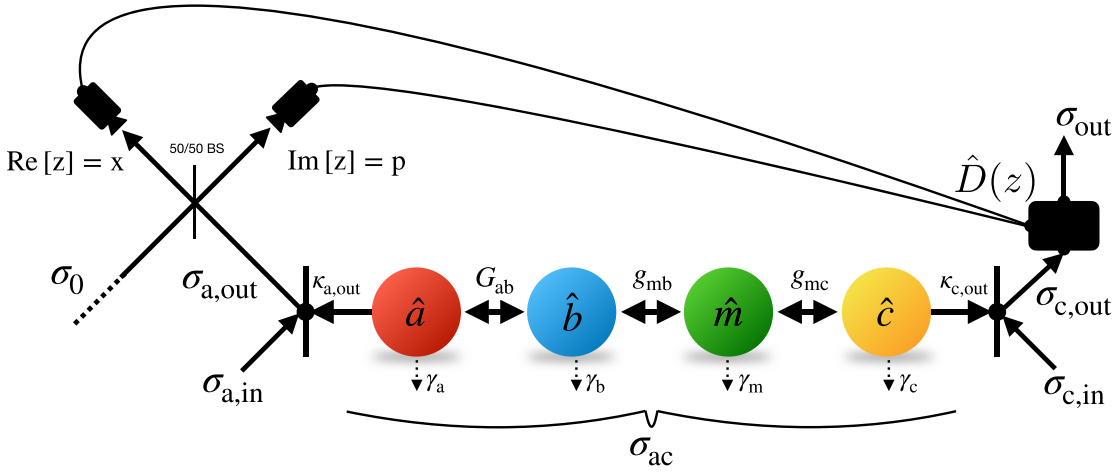

Figure 5. Sketch of the VBK transfer scheme [9, 10]. The coupled chain, containing optical photons ($\hat{a}$), phonons ($\hat{b}$), magnons ($\hat{m}$) and microwaves ($\hat{c}$) generates a two-mode optics-microwave squeezed state σ_{ac}. Teleportation of a state σ_0 consists on performing a displacement in the output microwave σ_{out} conditioned on the result of a homodyne detection in the optical part, indicated by the amplitude z.

4.2. Teleportation fidelity

For the teleportation of a coherent Gaussian state σ_0, the teleportation fidelity of the VBK scheme can be calculated (see appendix E for a detailed derivation) as

$$F = \frac{2}{\sqrt{\det(\sigma_0)\det(\sigma_{out})\det(\sigma_0+\sigma_{out})}}. \tag{15}$$

Besides depending on the state to be teleported σ_0, the fidelity is characterized by the covariance matrix σ_{out} (compare equation (E15)) of the output of the magnomechanical system, which, in turn, depends on the amount of entanglement generated. Thermal noise is most detrimental to the entanglement generation, as it causes destruction of the delicate quantum states. In contrast to the optical two-mode squeezed state in the original VBK proposal, our system is especially prone to thermal effects, since three of the four modes operate in the microwave frequency regime where thermal occupation at temperatures above zero is expected to cause significant decoherence. In the following we quantify the generated output steady-state entanglement as a function of temperature with a special emphasis on the ratio of internal to external dissipation rates at the two ports of our setup.

In figures 6(a) and (b) we plot both the output logarithmic negativity, and the teleportation fidelity for a coherent state, as a function of thermal occupation. We chose this state because it is the Gaussian state with minimal uncertainty and is of special interest for applications in quantum optics and quantum information. For the case of no internal dissipation of optical and microwave modes, we observe that at around $n_{th} \approx 105$ (corresponding to about 50.6 K at 10 GHz) the teleportation fidelity surpasses 0.5 for the optimum case with no internal dissipation of microwave and optical photon modes. This point signifies an improvement over the best fully classical local approach [99]. When internal dissipation is considered, entanglement starts to be generated at lower thermal occupations, and the fidelity is increased in a even smaller temperature region (on the order of a few 100 mK at 10 GHz). This suggests that internal mode dissipation at the port sites leads to much reduced teleportation fidelity even when entanglement is generated, an effect linked to the impact of port coupling efficiency.

In figure 6(c) we plot the teleportation fidelity as a function of the optical port coupling efficiency for three different values of the microwave port coupling efficiency at zero temperature. We observe a rapid decline of fidelity when either one of the port coupling efficiencies deviates from being equal to the other. For example, the port coupling efficiencies for the dashed curve in figure 6(b) are $\eta_a = 0.91$ and $\eta_c = 0.99$ which reduces the maximally achievable fidelity to about 0.82. Furthermore, figure 6(c) reveals that the teleportation fidelity can be optimized for reduced port coupling efficiencies, as long as they are matching. This implies a more complicated dependency of the entanglement generation on the port coupling efficiencies compared to the classical frequency conversion efficiency, which is just linearly dependent on $\eta_{a,c}$ [59]. The results also depend on the respective total linewidths of optical and microwave photon modes, which in turn are subject to the conditions on the cooperativities for maximizing entanglement discussed in the previous section. In figure 12 of appendix E we further show the fidelity for squeezed states as a function of the logarithmic negativity. Our results suggest that in our

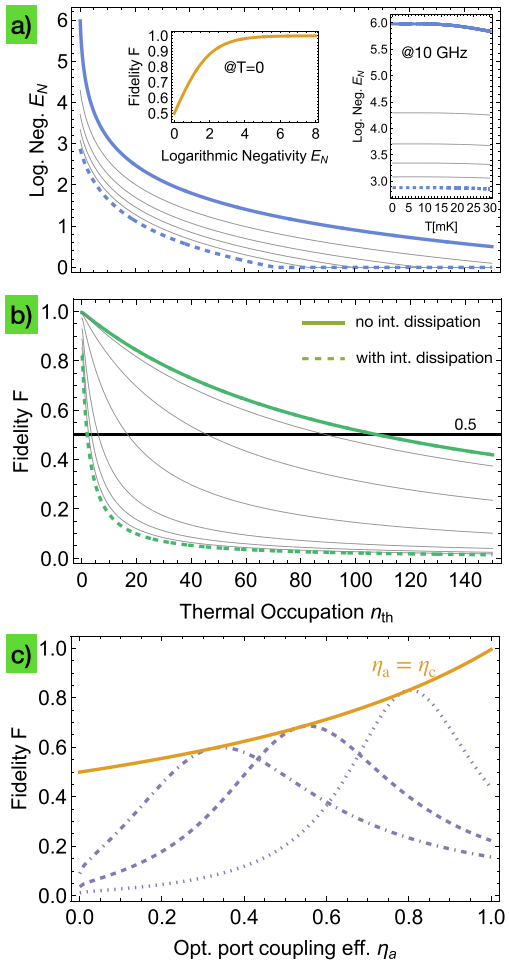

Figure 6. Logarithmic negativity (a) and teleportation fidelity (b) of an coherent state as a function of temperature, without (solid) and with (dashed) internal mode dissipation of optics and microwave, set to $\gamma_{a,\,\mathrm{int}} = 1\,\mathrm{GHz}$ and $\gamma_{c,\,\mathrm{int}} = 1\,\mathrm{MHz}$, respectively. The left inlet in plot (a) shows the fidelity of teleporting a coherent state as a function of logarithmic negativity at zero temperature. The right inlet shows low-temperature entanglement results for $-\Delta = \omega_{b/m/c} = 10\,\mathrm{GHz}$. The gray plot lines in (a) and (b) indicate increasing values of the internal dissipation rates $\gamma_{a/c,\,\mathrm{int}}$ from 0 to the values mentioned above. (c) State teleportation fidelity for a coherent state as a function of the optical port coupling efficiency η_a. It is obtained by fixing the total linewidths $\gamma_{a/c,\,\mathrm{tot}} = \gamma_{a/c,\,\mathrm{int}} + \kappa_{a/c}$, out $= 1.1\,\mathrm{GHz}/100.1$ MHz and putting $\alpha = 42$. The purple lines corresponds to different fixed values of the microwave port coupling efficiency $\eta_c = 0.35, 0.55, 0.8$. The orange line is obtained by setting $\eta_a = \eta_c$.

setup, teleportation of squeezed states can be achieved at a reduced fidelity at a given E_N. Regarding setup imperfections, temperature and internal dissipation rates are the most detrimental to the achievable entanglement.

5. Implementation in a magnomechanical disk

We now assess the implementation of the state teleportation scheme in a YIG disk, a promising geometry for tailoring the resonant magnon-phonon coupling [100]. Disks geometries have also been recently fabricated and experimentally probed [66–70]. For this proposed geometry, a realistic set of parameters is given in table 2, based on simulations and calculations presented in appendix G. We consider a YIG disk with radius $3.7\,\mu\mathrm{m}$, thickness 200 nm and with a hole of 400 nm mounted on a stem, see figure 1. The disk hosts optical whispering gallery modes (WGMs), which can couple to the evanescent light field of an optical fiber placed near its edge, that serves as an optical output port. The last component of the device is a microwave ring resonator, whose microwave field couples to the magnetic excitations of the disk. For this parameter regime, and in the following analysis, the system is always linearly stable because of the relatively weak coupling rates and large dissipation rates.

Compared to [100], we choose a two-times thicker disk, which improves the optomechanical interaction strength, our main source of entanglement. Based on our numerics (see figure 14(c) of appendix G), we expect an optimized single-photon optomechanical coupling rate of about 1 kHz, for

Table 2. Values for mode frequencies, linewidths/dissipations and coupling strengths for the proposed disk geometry.

Quantity	Symbol	Value
Optical photon freq.	$\omega_a/2\pi$	193.5 THz
Optical detuning (blue)	$\Delta_a/2\pi$	0.567 GHz
Phonon freq.	$\omega_b/2\pi$	0.567 GHz
Magnon freq.	$\omega_m/2\pi$	0.567 GHz
Microwave freq.	$\omega_c/2\pi$	0.567 GHz
Internal optical linewidth	$\gamma_a/2\pi$	0.001 THz
External optical dissipation	$\kappa_{a,\mathrm{out}}/2\pi$	0.099 THz
Phonon linewidth	$\gamma_b/2\pi$	5 kHz
Magnon linewidth	$\gamma_m/2\pi$	5 MHz
Internal mw cavity loss rate	$\gamma_c/2\pi$	0.01 MHz
External mw cavity coupling rate	$\kappa_{c,\mathrm{out}}/2\pi$	0.99 MHz
Magnomechanical coupling	$g_{mb}/2\pi$	5 MHz
Magnon-Microwave photon coupling	$g_{mc}/2\pi$	10 MHz
Optomechanical coupling	$g_{ab}/2\pi$	1.0 kHz
Optomechanical coop. (base value)	C_{ab}	8×10^{-9}
Magnomechanical coop.	C_{mb}	4000
Magon-microwave coop.	C_{mc}	80

the only azimuthal telecom wavelength WGM with mode number $m = 20$ and a radially symmetric mechanical breathing mode, which have been identified as the optimal modes for the protocol [100]. The increased thickness slightly lowers the magnomechanical coupling rate compared to the optimal result, to 5 MHz for a magnetic vortex breathing mode. In terms of the inductive magnon-microwave coupling, a mode volume overlap of 0.01% already suffices to obtain a coupling rate on the order of 10 MHz [59]. Based on estimates given in appendix G, see equation (G6), we choose the coupling rate to be 8 MHz. For the bare optical mode we assume 1550 nm telecom-wavelength photons, corresponding to a frequency 193.5 THz. For the protocol the cavity should be driven blue detuned by the frequency of the phonon mode. The mechanical mode frequency is fixed by the geometry and sets the necessary frequencies for all other modes in the system, including the optical detuning. The magnon mode frequency is tunable by an external magnetic field. Our numerical analysis performed as in [100] indicates that for this geometry and given dimensions, we can set all modes to resonance at 0.567 GHz for an optimized working point.

In a disk geometry, the optomagnonic coupling g_{am} can reach the kHz regime [94, 101]. Nevertheless, such a regime is strongly dependent on the geometrical parameters and the modes involved in the interaction. Under optimal mode-matching conditions for both modes, we can estimate the optomagnonic coupling for our proposed geometry as $g_{am} \sim 30$ kHz. Nevertheless, in a real device, optimizing both the optomechanical and optomagnonic couplings simultaneously would be challenging. In fact, even in proposals that are aimed at optimizing g_{am}, imperfect mode overlap is one of the main limiting factors for the coupling [93, 101–103]. A very optimistic reduction of g_{am} to 10 % of its optimal value due would already put it in the regime $g_{am} \sim g_{ab}$. Therefore, following the analysis in appendix C, we neglect a possible optomagnonic coupling in the rest of the manuscript.

Concerning the dissipative behavior of the modes, we resort again to numerical analysis and to estimates based on the literature. For optical modes at telecom frequency, our numerically obtained Q-factor is approximately 2700, corresponding to a total linewidth of about 0.1 THz (see figure 14(b) of appendix G). This puts the setup outside of the resolved sideband regime, since $\omega_b < \gamma_{a,\mathrm{tot}}$. In this regime, the interaction that generates entanglement, a two-mode squeezing interaction between the optical mode and the phonon mode, cannot be addressed perfectly, which furthers reduces the achievable entanglement. We assume a split of this total linewidth into an intrinsic part of the cavity mode itself (e.g. due to absorption), and an external part to the output optical fiber as $\gamma_{a,\mathrm{tot}} = \gamma_a + \kappa_{a,\mathrm{ext}} = 0.001\,\mathrm{THz} + 0.099\,\mathrm{THz}$, which can be justified based on the very low optical absorption of YIG in the telecom wavelength regime [104, 105]. This overcoupling of the optical port ensures optimal results for the entanglement generation, as has been discussed in the previous section. Based only on these numbers, we have $C_{ab} \approx 10^{-8}$, thus a very strong optical drive is required to enable significant entanglement generation. The dissipation of the magnon mode is determined by the Gilbert damping, and is expected for YIG microstructures to be on the order of 5 MHz [57]. Quality factors for mechanical modes in YIG disks are yet to be measured, however based on published results in similar silicon based geometries [106, 107], we assume a mechanical linewidth on the order of 5 kHz, yielding $C_{mb} = 4000$. Lastly, for

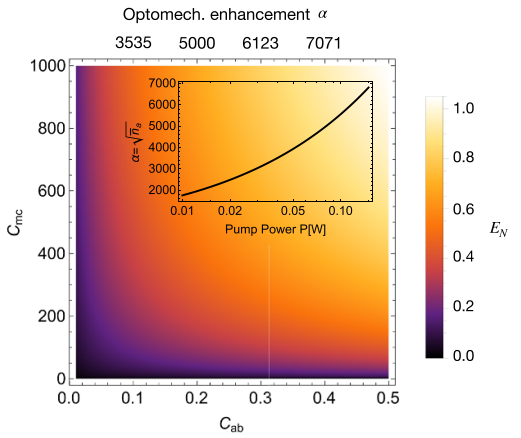

Figure 7. Steady state entanglement as a function of optomechanical (C_{ab}) and magnon-microwave (C_{mc}) cooperativity, for the proposed disk-based setup. The magnomechanical cooperativity was set, based on numerical analysis, to $C_{mb} = 4000$. The inlet shows the enhancement factor α as a function of the pump power. The upper scale shows the factor α for three values of C_{ab}. The values of the relevant parameters are given in table 2.

the microwave resonator we assume a total linewidth $\gamma_{c,\,\mathrm{tot}} = 1\,\mathrm{MHz}$ with a split between intrinsic and external as $\gamma_c + \kappa_{c,\,\mathrm{ext}} = 0.01\,\mathrm{MHz} + 0.99\,\mathrm{MHz}$. Planar ring resonators can exhibit high internal quality factors [108], which allows the operation of the resonator in the overcoupling regime via proper designing its coupling to the output ports. This numerical values yield the magnon-microwave cooperativity $C_{mc} = 80$, which can be tuned further in experiment, for example by adjusting the distance between resonator and disk, which yields a larger coupling due to better mode overlap.

Given the above considerations, we display in figure 7 the result for steady-state logarithmic negativity as function of both the optomechanical and magnon-microwave cooperativity. The primer can be controlled by the optical drive power, while the latter is mostly determined by mode overlap set by the distance between the split-ring resonator and the magnetic disk. Even though the optomechanical cooperativity is very low due to the small expected single-photon coupling, a logarithmic negativity of $E_N \approx 1$ can be achieved within a reasonable parameter space. Such an amount of entanglement corresponds to a teleportation fidelity of $F \approx 0.75$, as benchmarked in figure 12.

6. Conclusions and Outlook

We investigated the output entanglement between optical and microwave modes using a resonantly coupled magnomechanical hybrid system as mediator. The system combines resonant magnon-phonon and magnon-microwave couplings with the radiation pressure interaction between optical photons and phonons. The entanglement generated by a blue-detuned driven optomechanical interaction is maximized by pushing the system towards instability, with maximum entanglement obtained without the requirement of matching cooperativities. This allows for a flexibility in the system's design not present in other platforms. Interestingly, such a parameter regime coincides with the optimal frequency conversion regime obtained in a previous work [59].

The entanglement between output microwaves and optical photons was benchmarked by assessing the system's performance for continuous variable state teleportation. We have considered the scheme by VBK, which has the major advantage of not relying on any temporal control of the couplings for dark-state generation. Our analysis predicts that unit fidelities can be achieved in optimal systems for transferring coherent states at dilution fridge temperatures. Coherent state teleportation sets an important benchmark for potential advantages of using entangled states for quantum information tasks [99], such as teleportation of non-Gaussian states. Here, an important aspect is the impact of port-coupling efficiency which must be matched for optimal results. Besides the system design, such a scheme requires only standard tools, such as homodyne measurements and displacement operations, that are available both in the optical and in the microwave regime.

To asses the feasibility of the protocol on a realistic device, motivated by recent developments [66–70, 100, 109, 110], we proposed a device based on a mounted YIG-microdisk geometry where our protocol can be implemented. Using both numerical simulations and estimates for coupling strengths and

linewidths, we predict a fidelity of up to 0.75 for coherent state teleportation. The corresponding maximum output entanglement is on the order of $E_N \approx 1$, which outperforms the current experimentally achieved value of $E_N \approx 0.17$ [31]. Our analysis assumes noiseless operation of all the measurement apparatuses, which is an idealization. Under real conditions, added noise in the measurement chain would further reduced the amount of useful entanglement. This could be mitigated by exploring more efficient designs, such as microstructured crystals, which already have been fabricated and probed [62]. Furthermore, assuming a large mechanical Q-factor ensures entanglement generation at reasonable optical pump powers, even though the base-value of the optomechanical cooperativity remains small. Once such devices are properly optimized, we expect that its optomechanical coupling can reach that of similar devices fabricated with silicon [111], yielding results that are much closer to our predicted theoretical optimum.

Our proposed protocol represents a timely application of magnomechanical interaction for quantum information. The unique tunability of the magnons together with their strong resonant interaction with phonons in optimized geometries renders magnomechanical hybrid systems a promising platform for mediating the large frequency gap between optical and microwave frequencies, facilitating core tasks of quantum information processing. Recent experiments [58, 60] performed on bilayer structures at temperatures in the single Kelvin range further show the growing interest of operating magnomechanical systems in the quantum regime, or more precisely, in a regime where entanglement can be generated. A natural extension of this work would be to generalize the discussion to non-Gaussian states, such as superposition states. Even though calculations are equivalent for these states, analytical expressions for e.g. the fidelity are unlikely to be obtained and a numerical analysis is needed. Finally, the large generated output entanglement also goes alongside symmetric steerability (appendix F), which guarantees efficient distribution of entanglement among the constituents of our setup and enables implementation of other information protocols such quantum key distribution.

Acknowledgment

We thank Stefano Chesi, Sanchar Sharma, Benjamin Pigeau and Olivier Klein for very useful discussions. This work was supported by the EU-project HORIZON-EIC-2021-PATHFINDER OPEN PALANTIRI-101046630. F. E. and S.V.K. also acknowledge partial financial support by the Federal Ministry of Research, Technology and Space (BMFTR) project QECHQS (Grant No. 16KIS1590K).

Data availability statement

All data that support the findings of this study are included within the article (and any supplementary files).

Appendix A. Langevin equations

The parameters used in the main text are summarized in table 1. They are virtually identical to the ones used in [59]. The mean photon number in the optical cavity $\bar{n}_a$ can be estimated by

$$\bar{n}_a = \frac{\kappa_{a,\mathrm{out}} P}{\hbar\omega_a \left[\Delta_a^2 + (\gamma_a + \kappa_{a,\mathrm{out}})^2/4\right]}, \tag{A1}$$

where P is the drive power, γ_a the internal optical mode linewidth, $\kappa_{a,\mathrm{out}}$ the dissipation rate to the external port (see figure 8). We adopt the notation $\delta\hat{a} \to \hat{a}$. The quantum Langevin equations for the bosonic annihilation operators are obtained in the usual way via the Heisenberg equation of motion $\dot{\hat{o}}(t) = -\mathrm{i}[\hat{o}, \hat{H}]/\hbar$ (for an arbitrary bosonic operator $\hat{o}$), as

$$\begin{aligned}\dot{\hat{a}}(t) =& \mathrm{i}\Delta - \frac{\gamma_a + \kappa_{a,\mathrm{out}}}{2}\hat{a} - \mathrm{i}G_{ab}\left(\hat{b} + \hat{b}^\dagger\right) \\ & - \sqrt{\kappa_a}\hat{a}_{\mathrm{in}}(t), \end{aligned} \tag{A2a}$$

$$\begin{aligned}\dot{\hat{b}}(t) =& -\mathrm{i}\omega_b - \frac{\gamma_b}{2}\hat{b} - \mathrm{i}G_{ab}\left(\hat{a} + \hat{a}^\dagger\right) - \mathrm{i}g_{mb}\hat{m} \\ & - \sqrt{\gamma_b}\hat{b}_{\mathrm{in}}(t), \end{aligned} \tag{A2b}$$

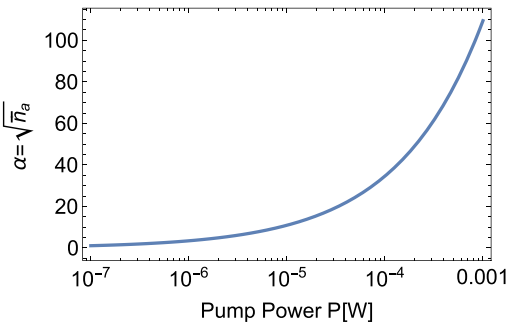

Figure 8. Plot of the square root of equation (A1) as a function of the optical pump power using parameters from table 1.

$$\dot{\hat{m}}(t) = -\mathrm{i}\omega_m - \frac{\gamma_m}{2}\hat{m} - \mathrm{i}g_{mb}\hat{b} - \mathrm{i}g_{mc}\hat{c} - \sqrt{\gamma_m}\hat{m}_{\mathrm{in}}(t), \tag{A2c}$$

$$\dot{\hat{c}}(t) = -\mathrm{i}\omega_c - \frac{\gamma_c + \kappa_{c,\mathrm{out}}}{2}\hat{c} - \mathrm{i}g_{mc}\hat{m} - \sqrt{\kappa_c}\hat{c}_{\mathrm{in}}(t). \tag{A2d}$$

These equations can be cast in the from of equation (5) in the main text by using vectors

$$\hat{\mathbf{A}} = \left(\hat{a}^\dagger, \hat{a}, \hat{b}^\dagger, \hat{b}, \hat{m}^\dagger, \hat{m}, \hat{c}^\dagger, \hat{c}\right)^{\mathrm{T}}, \tag{A3}$$

and

$$\hat{\mathbf{A}}_{\mathrm{in}} = \left(\hat{a}^\dagger_{\mathrm{out}}, \hat{a}_{\mathrm{out}}, \hat{a}^\dagger_{\mathrm{in}}, \hat{a}_{\mathrm{in}}, \hat{b}^\dagger_{\mathrm{in}}, \hat{b}_{\mathrm{in}}, \hat{m}^\dagger_{\mathrm{in}}, \hat{m}_{\mathrm{in}}, \hat{c}_{\mathrm{out}}, \hat{c}^\dagger_{\mathrm{out}}, \hat{c}^\dagger_{\mathrm{in}}, \hat{c}_{\mathrm{in}}\right)^{\mathrm{T}}. \tag{A4}$$

The transformation matrix connecting the bare mode operators $\hat{\mathbf{A}}$ with the quadrature operators $\hat{\mathbf{R}}$ via $\hat{\mathbf{R}} = Q\hat{\mathbf{A}}$. Recall that the quadratures are defined here as

$$\begin{aligned} \hat{x}_a &= \hat{a} + \hat{a}^\dagger, \\ \hat{p}_a &= \mathrm{i}\left(\hat{a}^\dagger - \hat{a}\right). \end{aligned} \tag{A5}$$

hence the transformation matrix reads

$$Q = \mathbb{1}_6 \bigotimes \begin{pmatrix} 1 & \mathrm{i} \\ -\mathrm{i} & 1 \end{pmatrix} \tag{A6}$$

Appendix B. Stability analysis

Since the entanglement generation of this setup relies on the parametric interaction between optical light and mechanical modes, it is important to check that the system remains stable for the range of parameters used. We describe the dynamics of the setup by the linear matrix equation of equation (5). The system will be stable provided that the real parts of $\{\lambda_i\}$, the eigenvalues of $\mathbb{A}$, are negative. This guarantees that all solutions will be damped in time and hence are linearly stable. To delimit the stability regions shown in the plots of figures 4, we have numerically calculated the eigenvalues of $\mathbb{A}$ for the relevant set of parameters, and identified the stability regions as those in which $\mathrm{Re}[\lambda_i] < 0$ for all the eigenvalues. We now extend this analysis and plot stability diagrams for the system as a function of the optomechanical enhancement factor α and the magnon frequency ω_m as the tunable parameters that can put the system in an unstable regime.

In figure 9 we show the stable and unstable regions in the (α, ω_m) parameter space, for the same parameters used in figure 4. The system is more stable when the magnon mode is at resonance with the phonon and microwave modes as, in this case, excitations can be exchanged very efficiently to the microwave mode. Otherwise, figure 9(b) shows a larger stability range as a function of α, due to the lower value of the magnon-microwave coupling.

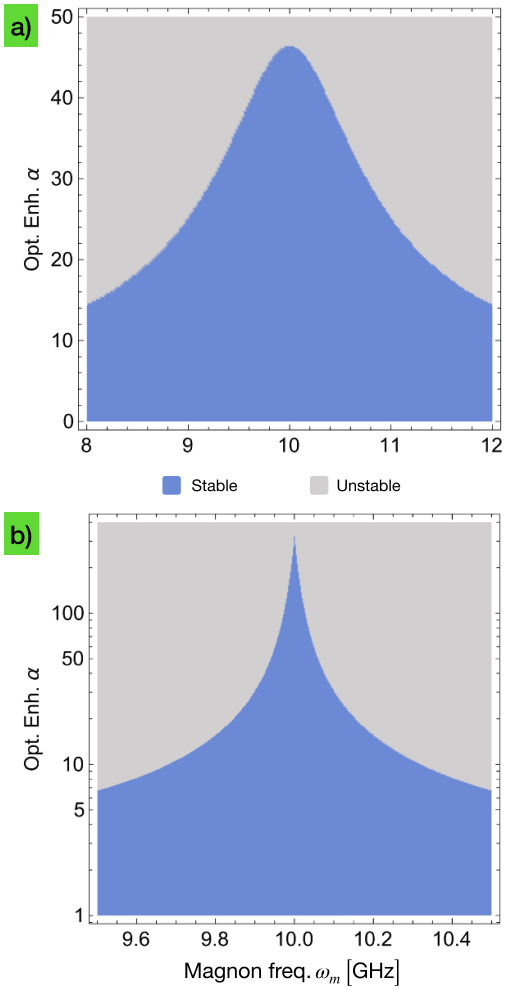

Figure 9. (a) Stability analysis based on the real part of the eigenvalues of the dynamical matrix $\mathbb{A}$ (see equation (5)) for parameters given in table 1 as a function of magnon frequency ω_m and optomechanical enhancement factor α. (b) Same analysis, except for a magnon-microwave coupling $g_{mc} = 18\,\mathrm{GHz}$.

The stability analysis for the parameters set of the disk geometry, given in table 2, revealed no regions of instability in any relevant parameter regime. The reason for that is the very large optical linewidth $\gamma_{a,\,\mathrm{tot}}$, which yields $\gamma_{a,\,\mathrm{tot}} \gg \alpha g_{ab}$ for any reasonable optical pump power as well as no sensitivity to magnon detuning. Inclusion of an additional optomagnonic interaction g_{am} also does not influence the stability properties of the setup, except for the rather unrealistic case of $g_{am} > 10 g_{ab}$.

Appendix C. Effect of a finite optomagnonic coupling

In this appendix we investigate the effect of including an optomagnonic interaction in the setup. To address this point, we have computed the optics-microwave output entanglement including in the Hamiltonian equation (1) the optomagnonic interaction [83, 95, 96]

$$\hat{H}_{am}/\hbar = g_{am}\hat{a}^\dagger\hat{a}\left(\hat{m} + \hat{m}^\dagger\right). \tag{C1}$$

The linearization of the system follows the same procedure, and will induce an additional magnon-photon interacting term that can also generate entanglement, depending on the optical detuning. We show the corresponding results for the optics-microwave entanglement in figures 10(a) and (b). In (a), we consider a narrow filter function, corresponding to the results of figure 4 in the main text, while in (b) we keep the magnon mode at resonance with the microwave and the phonon mode while varying the center frequency of the filter.

Overall, the results suggest that the optomagnonic coupling only has an appreciable impact in the output optics-microwave entanglement provided that $g_{am} > g_{ab}$ by at least an order of magnitude. For $g_{am} \sim g_{ab}$, there is a small difference when compared to the $g_{am} = 0$ case, in particular with respect to

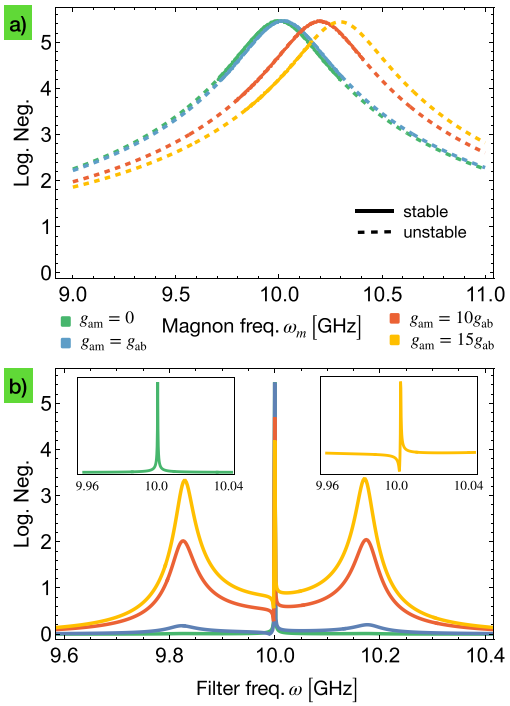

Figure 10. Impact of an optomagnonic interaction on the output entanglement generation. Figure (a) was made in accordance with figure 4(a) in the main text using the same set of parameters. In (b), the filter center frequency is varied instead while all other parameter follow table 1.

the frequency that maximizes the logarithmic negativity, but the entanglement has the same behavior as function of the magnon frequency. When the frequency of the filter is varied, we notice the emergence of a Fano-like resonance in the entanglement, observable only at large values of g_{ab}. This feature is due to an interference in difference paths that the generated excitations can take to be converted from optics to microwaves. We also notice that for $g_{am} > g_{ab}$ the stability region is reduced, due to enhanced generation of pairs of excitations.

The optomagnonic coupling $g_{am} = |g^F_{am} + g^{CM}_{am}|$ includes a contribution due to the Faraday effect g^F_{am} and due to the Cotton–Mouton effect g^{CM}_{am}. We can estimate the Faraday effect contribution in an idealized scenario, where the optical mode and the magnon mode have a perfect overlap by [93, 96]:

$$|g^F_{am}| = \frac{\theta_F \lambda_n}{2\pi} \omega_a \sqrt{\frac{g\mu_B}{M_S V_{\mathrm{mag}}}}, \tag{C2}$$

where θ_F is the Faraday rotation angle per unit length, λ_n is the wavelength of light inside the dielectric, g is the Landé factor, μ_B is the Bohr magneton, M_S is the saturation magnetization and V_{mag} is the volume of the magnet. Using the parameters for YIG, $\theta_F \lambda_n/(2\pi) \sim 4 \times 10^5$, $M_S = 140\,\mathrm{kA\,m^{-1}}$, and for a magnet with volume $V_{\mathrm{mag}} = 1\mu m^3$ (corresponding to the parameters of [59]), we obtain $|g^F_{am}|/2\pi \sim 0.1$ MHz. An estimate of $g^F_{am} + g^{CM}_{am}$ is more involved, as the relative phases of the couplings, which depends on the geometry of the system, can yield interference effects. Since the Cotton–Mouton coefficient $\theta_C \lambda_n$ is typically of the same order of the Faraday coefficient, we can estimate $|g_{am}| \sim |g_{ab}|$ (see table 1).

For our proposed disk geometry, the same estimate yields $g_{am} \sim 30$ kHz assuming a perfect overlap between the optical mode and the magnon mode. Even in the proposal of [93], the best optimized overlap between modes would cause a reduction of 4 % of the optomagnonic coupling. This is also the case in practical setups, such as [102, 103], in which the reduction is even more drastic. Since the value of g_{ab} shown in the table 2 of the main text does take into account imperfect mode overlap, a fair comparison between g_{am} and g_{ab} for our proposed setup should also include such a mismatch. A reduction to 10 % of the optimal value of g_{am} would already put $g_{am} \sim g_{ab}$.

Although the inclusion of the optomagnonic coupling and the resulting effects are interesting and could apply to other geometries, we conclude that we can safely discard any contribution of g_{am} for the entanglement generation for the disk geometry considered in our work.

Appendix D. Covariance matrix in the frequency domain

Our aim is to obtain the covariance matrix for the optics and microwave output in frequency space. In general, the elements of the covariance matrix in frequency space are given by

$$\sigma_{ij}^{\text{intra}}[\omega] = \frac{1}{2}\int_{-\infty}^{\infty} \mathrm{d}\omega' \langle \{\hat{R}_i[\omega], \hat{R}_j[\omega']\}\rangle , \tag{D1}$$

where $\{\}$ is the anti-commutator and where we can already assume a vacuum ground state, so $\langle \hat{R}_i\rangle\langle \hat{R}_j\rangle = 0$. In the next step we conveniently write

$$\sigma^{\text{intra}}[\omega] = \frac{1}{2}\int_{-\infty}^{\infty} \mathrm{d}\omega' \left\langle \hat{\mathbf{R}}[\omega]\hat{\mathbf{R}}^T[\omega'] + \left(\hat{\mathbf{R}}[\omega]\hat{\mathbf{R}}^T[\omega']\right)^T \right\rangle . \tag{D2}$$

Since we want to quantify the output entanglement, we set $\hat{\mathbf{R}} = \hat{\mathbf{R}}_{\text{out}}$. The output and input quadratures are connected by a scattering-matrix via $\hat{\mathbf{R}}_{\text{out}} = S_{\mathbf{R}}[\omega]\hat{\mathbf{R}}_{\text{in}}$. For the bare modes $\hat{\mathbf{A}}$, the scattering matrix is obtained by input-output relations $\hat{\mathbf{A}}_{\text{out}} = \hat{\mathbf{A}}_{\text{in}} + \mathbb{B}\hat{\mathbf{A}}$ leading to $S_{\mathbf{A}}[\omega] = \mathbb{B}^T(\mathrm{i}\omega\mathbb{1}_8 + \mathbb{A})^{-1}\mathbb{B} + \mathbb{1}_{12}$, where the matrices $\mathbb{A}$ and $\mathbb{B}$ are defined in equation (5). In the quadrature basis we then have $S_{\mathbf{R}}[\omega] = QS_{\mathbf{A}}[\omega]Q^{-1}$. With that we write the covariance matrix for the outputs as

$$\begin{aligned}\sigma^{\text{out}}[\omega] =& \frac{1}{2}\int_{-\infty}^{\infty} \mathrm{d}\omega' S_{\mathbf{R}}[\omega]\langle \hat{\mathbf{R}}_{\text{in}}[\omega]\hat{\mathbf{R}}_{\text{in}}^T[\omega']\rangle S_{\mathbf{R}}^T[\omega'] \\ &+ \frac{1}{2}\int_{-\infty}^{\infty} \mathrm{d}\omega' \left(S_{\mathbf{R}}[\omega]\langle \hat{\mathbf{R}}_{\text{in}}[\omega]\hat{\mathbf{R}}_{\text{in}}^T[\omega']\rangle S_{\mathbf{R}}^T[\omega']\right)^T .\end{aligned} \tag{D3}$$

This expression contains correlators of the input noise in the form $\langle \hat{\mathbf{R}}_{\text{in}}[\omega]\hat{\mathbf{R}}_{\text{in}}^T[\omega']\rangle = N_{\mathbf{R}}\delta(\omega+\omega')$. Therefore, the final expression for the output covariance matrix reads

$$\sigma^{\text{out}}[\omega] = \frac{1}{2}\left(S_{\mathbf{R}}[\omega]N_{\mathbf{R}}S_{\mathbf{R}}^T[-\omega] + S_{\mathbf{R}}[-\omega]N_{\mathbf{R}}^T S_{\mathbf{R}}^T[\omega]\right) , \tag{D4}$$

where

$$N_{\mathbf{R}} = \bigoplus_{j=a,b,m,c} \begin{pmatrix} 2n_{\text{th}}j+1 & \mathrm{i} \\ -\mathrm{i} & 2n_{\text{th}}j+1 \end{pmatrix} . \tag{D5}$$

Here, the (white) noise correlations in frequency space for the bare operators were used, defined as

$$\begin{aligned}\langle \hat{\beta}(\omega)\hat{\beta}^\dagger(\omega')\rangle &= (n_{\text{th},\beta}+1)\delta(\omega+\omega') , \\ \langle \hat{\beta}^\dagger(\omega)\hat{\beta}(\omega')\rangle &= n_{\text{th},\beta}\delta(\omega+\omega') ,\end{aligned} \tag{D6}$$

with $\hat{\beta} = \hat{a}_{\text{in}}, \hat{b}_{\text{in}}, \hat{m}_{\text{in}}, \hat{c}_{\text{in}}$. For the filter function in equation (13) we assume a Gaussian function with width σ, given by

$$f(\sigma,\omega'-\omega) = \frac{1}{\sqrt{\sigma\sqrt{\pi}}}\exp\left[-\frac{(\omega'-\omega)^2}{2\sigma^2}\right] . \tag{D7}$$

The dependence on the generated entanglement as a function of the filter bandwidth σ can be seen in figure 11. Next, the elements of the covariance matrix defined in equation (14) in terms of the cooperativites $C_{ij} = 4g_{ij}^2/\gamma_{i,\text{tot}}\gamma_{j,\text{tot}}$ are given as

$$\begin{aligned} c_1 &= \frac{C_{ab}^2(1+C_{mc})^2 + 6C_{ab}(1+C_{mc})(1+C_{mb}+C_{mc})(1+C_{mb}+C_{mc})^2}{(1+C_{mb}+C_{mc}-C_{ab}(1+C_{mc}))^2} , \\ c_2 &= \frac{C_{ab}^2(1+C_{mc})^2 + (1+C_{mb}+C_{mc})^2 - 2C_{ab}\left(C_{mb} - 3C_{mb}C_{mc} + (1+C_{mc})^2\right)}{(1+C_{mb}+C_{mc}-C_{ab}(1+C_{mc}))^2} , \\ c_3 &= \frac{4\sqrt{C_{ab}C_{mb}C_{mc}}(1+C_{ab}+C_{mb}+C_{mc}(1+C_{ab}))}{(1+C_{mb}+C_{mc}-C_{ab}(1+C_{mc}))^2} . \end{aligned} \tag{D8}$$

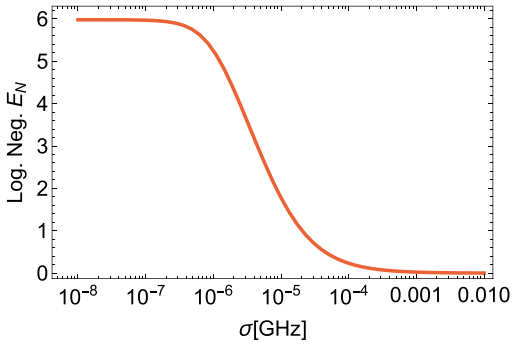

Figure 11. Generated output entanglement E_N as a function of the filter bandwidth σ.

Note that due to two stages between the output modes, the covariance matrix has rotated off-diagonal blocks compared to the standard TMS covariance matrix, that is obtained for one-stage setups. More generally, the output covariance matrix takes the form

$$\sigma^{ij}_{\text{general}} = \begin{pmatrix} a_1 & 0 & a_4 & a_3 \\ 0 & a_1 & a_3 & -a_4 \\ a_4 & a_3 & a_2 & 0 \\ a_3 & -a_4 & 0 & a_2 \end{pmatrix} , \tag{D9}$$

where the a_i are real numbers. Based on equations (10) and (11) we have

$$\Sigma = a_1^2 + a_2^2 + 2\left(a_3^2 + a_4^2\right) ,$$

$$\det\sigma = \left(-a_1 a_2 + a_3^2 + a_4^2\right)^2 , \tag{D10}$$

and

$$\eta_- = \frac{1}{\sqrt{2}}\left(a_1^2 + a_2^2 + 2\left(a_3^2 + a_4^2\right) - |a_1 + a_2|\left(\left(a_1 - a_2\right)^2 + 4\left(a_3^2 + a_4^2\right)\right)^{1/2}\right)^{1/2} . \tag{D11}$$

Appendix E. Teleportation fidelity

In this appendix we show the detailed derivation of the teleportation fidelity for coherent states. For the first part, we follow the first steps of [99] and then calculate an analytical expression for the output Wigner function that does not contain any further integration. This can only be done when we consider purely states with Gaussian statistics, that are fully characterized by their covariance matrix. The teleportation is then obtained by comparing the overlap of the input and output Wigner function. Note that in the following, our notation is not specific for the system in the main text. For optics-to-microwave teleportation, one would have indices $2, 3 = \hat{a}, \hat{c}$ for $\mathbf{x}_2$ and $\mathbf{x}_3$. The Wigner function of the output state is then given by

$$W_{\text{out}}(\mathbf{x}_0, \mathbf{x}_3) = \int dx_z \mathrm{d}p_z dx_2 dp_2 W[\sigma_0](x_z + x_2, p_z - p_2) \\ W[\sigma_{23}](x_2, p_2, x_3 - x_z, p_3 - p_z) . \tag{E1}$$

The output Wigner function only depends on the phase space coordinates of the output state at $\mathbf{x}_3$, which in our model would be, for example, the microwave output port. The integration over the coordinates $\mathbf{x}_2$ and $\mathbf{x}_z$ covers all possible outcomes of the joint measurement performed at the input point (in our model the optical port). The z-coordinates come from a double-homodyne density probability distribution $p(z)$, considering the kind of joint measurement that can be performed on two optical states.

The Wigner function of the coherent input state (to be teleported) is given by

$$W_0\left(x_z+x_2,p_z-p_2\right)=\exp\left(-\frac{1}{2}\left(\mathbf{x}_2^T\sigma_z+\mathbf{x}_z^T-\mathbf{x}_0^T\right)\sigma_0^{-1}\left(\sigma_z\mathbf{x}_2+\mathbf{x}_z-\mathbf{x}_0\right)\right)\frac{1}{2\pi\sqrt{\det\left(\sigma_0\right)}}, \tag{E2}$$

where we included a displacement vector $\mathbf{x}_0$ and where σ_z is the Pauli-z matrix. We further introduced the notation $\mathbf{x}_2=\left(x_2,p_2\right)^T$. For the Wigner function of the entangled output-pair, we first decompose its covariance matrix σ_{23} into four blocks via $\sigma_{23}^{-1}=\begin{pmatrix}\mathbb{A}_2 & \mathbb{A}_{23}\\ \mathbb{A}_{32} & \mathbb{A}_3\end{pmatrix}$. The resulting Wigner function is given by

$$W_{23}\left(x_2,p_2,x_3-x_z,p_3-p_z\right)=\exp\left(-\frac{1}{2}\left(\mathbf{x}_2^T\mathbb{A}_2\mathbf{x}_2+\mathbf{x}_2^T\mathbb{A}_{23}\left(\mathbf{x}_3-\mathbf{x}_z\right)+\left(\mathbf{x}_3^T-\mathbf{x}_z^T\right)\mathbb{A}_{32}\mathbf{x}_2+\left(\mathbf{x}_3^T-\mathbf{x}_z^T\right)\mathbb{A}_3\left(\mathbf{x}_3-\mathbf{x}_z\right)\right)\right)\frac{1}{\left(2\pi\right)^2\sqrt{\det\left(\sigma_{23}\right)}}. \tag{E3}$$

By defining the vector $\mathbf{x}_{2z}=\mathbf{x}_2\bigoplus\mathbf{x}_z$ we can group the terms in equations (E2) and (E3) conveniently together to obtain

$$W_{\text{out}}\left(\mathbf{x}_0,\mathbf{x}_3\right)=\frac{1}{\left(2\pi\right)^3\sqrt{\det\sigma_0\det\sigma_{23}}}\exp\left(-\frac{1}{2}\left(\mathbf{x}_3^T\mathbb{A}_3\mathbf{x}_3+\mathbf{x}_0^T\sigma_0\mathbf{x}_0\right)\right)\int\mathrm{d}x_z\mathrm{d}p_z\mathrm{d}x_2\mathrm{d}p_2\exp\left(\frac{1}{2}\left(\mathbf{x}_{2z}^T\mathbb{Q}_{2z}\mathbf{x}_{2z}+\left(\mathbf{A}_{2z}^T+\mathbf{B}_{2z}^T\right)\mathbf{x}_{2z}\right)\right), \tag{E4}$$

where we have defined the matrix

$$\mathbb{Q}_{2z}=\begin{pmatrix}\mathbb{A}_2+\sigma_z\sigma_0\sigma_z & -\mathbb{A}_{23}+\sigma_z\sigma_0\\ -\mathbb{A}_{23}+\sigma_0\sigma_z & \mathbb{A}_3+\sigma_0\end{pmatrix}, \tag{E5}$$

and the two vectors

$$\mathbf{A}_{2z}=\begin{pmatrix}\mathbb{A}_{23}\mathbf{x}_3-\sigma_z\sigma_0\mathbf{x}_0\\ -\mathbb{A}_3\mathbf{x}_3-\sigma_0\mathbf{x}_0\end{pmatrix}, \tag{E6}$$

and

$$\mathbf{B}_{2z}=\begin{pmatrix}\mathbb{A}_{32}^T\mathbf{x}_3-\sigma_z\sigma_0^T\mathbf{x}_0\\ -\mathbb{A}_3^T\mathbf{x}_3-\sigma_0^T\mathbf{x}_0\end{pmatrix}. \tag{E7}$$

In the next step we can carry out the integral in equation (E4) by using the identity for a multi-dimensional Gaussian integral with additional linear term. The final result is

$$W_{\text{out}}\left(\mathbf{x}_0,\mathbf{x}_3\right)=\frac{1}{2\pi\sqrt{\det\left(\sigma_0\right)\det\left(\sigma_{23}\right)\det\left(\mathbb{Q}_{2z}\right)}}\exp\left(-\frac{1}{2}\left(\mathbf{x}_3^T\mathbb{A}_3\mathbf{x}_3+\mathbf{x}_0^T\sigma_0\mathbf{x}_0\right)\right)\exp\left(\frac{1}{2}\left(\mathbf{A}_{2z}+\mathbf{B}_{2z}\right)\mathbb{Q}_{2z}^{-1}\left(\mathbf{A}_{2z}^T+\mathbf{B}_{2z}^T\right)\right). \tag{E8}$$

The teleportation fidelity for coherent states can be calculated via

$$F=4\pi\int\mathrm{d}\mathbf{x}_3W_{\text{out}}\left(\mathbf{x}_0,\mathbf{x}_3\right)W[\sigma_0]\left(\mathbf{x}_0,\mathbf{x}_3\right). \tag{E9}$$

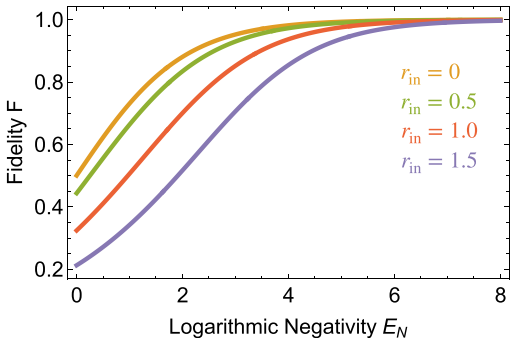

Figure 12. Teleportation fidelity as a function of logarithmic negativity calculated based on the TMS covariance matrix in equation (E16). The colors indicate different squeezing factors r_{in} of the state to be teleported.

Using equations (E2) and (E8). In order to carry out the integration we decompose the second exponential in equation (E8) in the form

$$W_{out}(\mathbf{x}_0, \mathbf{x}_3) = \frac{1}{2\pi\sqrt{\det(\sigma_0)\det(\sigma_{23})\det(\mathbb{Q}_{2z})}} \exp\left(-\frac{1}{2}\left(\mathbf{x}_3^T\mathbf{A}\mathbf{x}_3 + \mathbf{x}_0^T\mathbf{B}\mathbf{x}_3 + \mathbf{x}_0^T\mathbf{C}\mathbf{x}_0\right)\right), \tag{E10}$$

where we defined

$$\begin{aligned}\mathbf{A} &= -\left(\mathbb{A}_{32}\mathbb{B}_2\mathbb{A}_{23} - \mathbb{A}_{32}\mathbb{B}_{23}\mathbb{A}_3 - \mathbb{A}_3\mathbb{B}_{32}\mathbb{A}_{23} + \mathbb{A}_3\mathbb{B}_3\mathbb{A}_3\right) + \mathbb{A}_3\\ \mathbf{B} &= -2\sigma_0\left(-\sigma_z\mathbb{B}_2\mathbb{A}_{23} - \mathbb{B}_{32}\mathbb{A}_{23} + \sigma_z\mathbb{B}_{23}\mathbb{A}_{23} + \mathbb{B}_3\mathbb{A}_3\right),\\ \mathbf{C} &= -\sigma_0\left(\sigma_z\mathbb{B}_2\sigma_z + \sigma_z\mathbb{B}_{23} + \mathbb{B}_{32}\sigma_z + \mathbb{B}_3\right)\sigma_0 + \sigma_0,\end{aligned} \tag{E11}$$

and used the elements of the matrix $\mathbb{Q}_{2z}^{-1} = \begin{pmatrix}\mathbb{B}_2 & \mathbb{B}_{23}\\ \mathbb{B}_{32} & \mathbb{B}_3\end{pmatrix}$. There exists an orthogonal transformation $\mathbf{U}$ ($\mathbf{U}^{-1} = \mathbf{U}^T$) such that $\mathbf{UB} = -2\mathbf{A}$ and $\mathbf{UCU}^{-1} = \mathbf{A}$. This transforms the exponent in equation (E10) via

$$\begin{aligned}\mathbf{x}_0^T\mathbf{B}\mathbf{x}_3 &= \mathbf{x}_0^T\mathbf{U}^{-1}\mathbf{U}\mathbf{B}\mathbf{x}_0 = -\mathbf{y}_0^T\mathbf{A}\mathbf{x}_3 - \mathbf{x}_3^T\mathbf{A}\mathbf{y}_0,\\ \mathbf{x}_0^T\mathbf{B}\mathbf{x}_0 &= \mathbf{x}_0^T\mathbf{U}^{-1}\mathbf{U}\mathbf{C}\mathbf{U}^{-1}\mathbf{U}\mathbf{x}_0 = \mathbf{y}_0^T\mathbf{A}\mathbf{y}_0,\end{aligned} \tag{E12}$$

and the fidelity integral becomes

$$F = \int \mathrm{d}(\mathbf{x}_3 - \mathbf{y}_0) \frac{4\pi}{(2\pi)^2\det(\sigma_0)\sqrt{\det(\sigma_{23})\det(\mathbb{Q}_{2z})}} \exp\left(-\frac{1}{2}\left((\mathbf{x}_3 - \mathbf{y}_0)^T\left(\mathbf{A} + \sigma_0^{-1}\right)(\mathbf{x}_3 - \mathbf{y}_0)\right)\right), \tag{E13}$$

which yields the result

$$F = \frac{2}{\det(\sigma_0)\sqrt{\det(\sigma_{23})\det(\mathbb{Q}_{2z})\det\left(\mathbf{A}^{-1} + \sigma_0\right)}}. \tag{E14}$$

Identifying $\det(\sigma_0)\det(\sigma_{23})\det(\mathbb{Q}_{2z}) = \det(\sigma_{out})$ and $\sigma_{out}^{-1} = \mathbf{A}$ gives equation (15) of the main text. Notice that all coherent states have the same teleportation fidelity, since the quantity depends only on the covariance matrix of the state to be transfered ω_0 and the amount of entanglement shared between the two modes used for the protocol. One can also recast the Wigner function of the output mode as

$$W_{out}(\mathbf{y}_0, \mathbf{x}_3) = \exp\left(-\frac{1}{2}(\mathbf{x}_3 - \mathbf{y}_0)^T\sigma_{out}^{-1}(\mathbf{x}_3 - \mathbf{y}_0)\right)\frac{1}{2\pi\sqrt{\det(\sigma_{out})}}. \tag{E15}$$

Note that the input vector transforms via $\mathbf{y}_0 = \mathbf{U}\mathbf{x}_0$ with $\mathbf{U} = -2\mathbf{A}\mathbf{B}^{-1}$. That simplifies the expression for the fidelity even further, and finally gives rise to equation (15) in the main text.

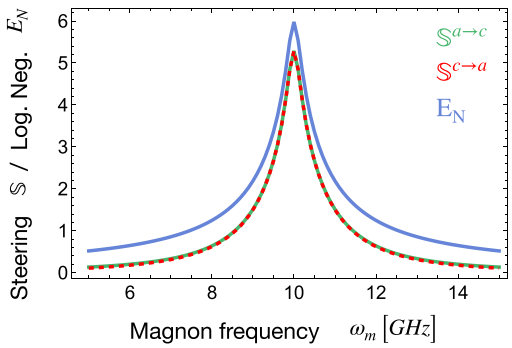

Figure 13. Quantification of quantum steering in both directions under optimal conditions alongside the generated logarithmic negativity. The temperature is set to zero, all other parameters follow table 1 with an optical drive enhancement of $\alpha = 42$.

For benchmarking the generated entanglement, we can compare to the covariance matrix of a twin-beam state exhibiting two-mode squeezing controlled by the parameter r

$$\sigma_{\mathrm{TMS}} = \begin{pmatrix} \cosh(2r) & 0 & \sinh(2r) & 0 \\ 0 & \cosh(2r) & 0 & -\sinh(2r) \\ \sinh(2r) & 0 & \cosh(2r) & 0 \\ 0 & -\sinh(2r) & 0 & \cosh(2r) \end{pmatrix}. \tag{E16}$$

We can use equation (E16) to benchmark the transfer fidelity as a function of the logarithmic negativity E_N. Results for different squeezed coherent input states are plotted in figure 12. The more squeezed the input state is, meaning the larger the squeezing factor r_{in} is chosen, the larger E_{N} of the setup that generates two-mode squeezing needs to be, in order to achieve high transfer fidelity.

Appendix F. Steering

An additional quantity of interest in terms of security is entanglement steering. This quantifies how much one party, say Alice, can influence the other party, Bob, by actions on her side. For continuous-variable systems described by a bipartite covariance matrix (compare equation (9)), it can be quantified as [112]

$$\mathbb{S} = \max\left\{0, S\left(B^{(\prime)}\right) - S\left(\sigma_{ij}\right)\right\}, \tag{F1}$$

where $S(\sigma) = \frac{1}{2}\ln(\det\sigma)$ is the Rényi-2 entropy function and where the use of either B or B' determines the steering of $\hat{a}$ on $\hat{c}$ or vice versa, respectively.

The plot in figure 13 shows the quantum steering in both directions under optimal conditions and zero temperature. We observe exactly what was reported in [112]. The steering is symmetric for the two-mode coherent state of our system and quantitatively always smaller than the logarithmic negativity. The maximum difference between the two quantities is about $\ln 2$.

Appendix G. Details on numerical results and estimates

In the following we give further details on the numerically obtained parameters used in section 5. Figure 14 contains the results that have been obtained based on numerical calculations. Figure 14(a) shows examples of spatial mode profiles that can be used, while (b) and (c) show results for the optical modes and quality factors, as well as the expected optomechanical coupling.

G.1. Microwave ring resonator

The microwave photons are considered to be contained in a LC circuit based resonator, which is described by a Hamiltonian of the form

$$\hat{H}_{\mathrm{LC}} = \hbar\omega_c\left(\hat{c}^\dagger\hat{c} + \frac{1}{2}\right). \tag{G1}$$

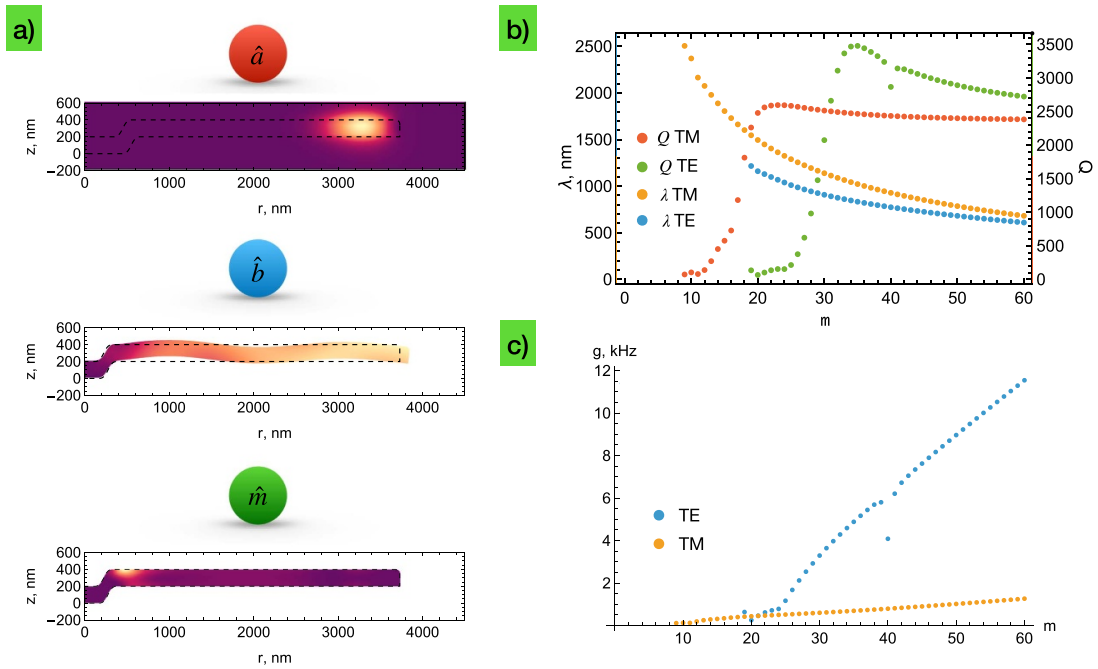

Figure 14. (a) Examples of spatial mode profiles for optical photon $\hat{a}$ (azimuthal WGM, $m = 20$ for telecom wavelength of $\approx 1550\,\mathrm{nm}$), phonon $\hat{b}$ (radially symmetric breathing mode) and magnon $\hat{m}$ (vortex breathing mode). (b) Optical mode wavelength λ and quality factor Q as a function of the azimuthal mode number m for both TE and TM. (c) Optomechanical coupling rate for TE and TM modes as a function of the azimuthal mode number m.

We quantize the interaction with the LC circuit using the charge-flux canonically conjugate variables. The interaction Hamiltonian is constructed solely based on the Zeeman interaction,

$$H_{\mathrm{Zeeman}} = \int \mathrm{d}r^3\, M(\mathbf{r}) \cdot B(\mathbf{r})\,, \tag{G2}$$

where the field of the coupling antenna is assumed to come from a ring of negligible thickness and width going around the nanostructure ($\approx 100\,\mathrm{nm}$) off of its side and at the height of the foot of the structure. The required field B can be found via the Biot–Savart law

$$\mathbf{B}(\mathbf{r}) = \frac{\mu_0}{4\pi} \int_U \frac{I[\mathrm{d}l \times \mathbf{r}']}{|\mathbf{r}'|^3}\,, \tag{G3}$$

where we integrate over a closed curve U. The current can be obtained in quantized form from the charge zero-point fluctuations and the Hamiltonian (G1)

$$\hat{I} = \frac{\mathrm{d}\hat{Q}}{\mathrm{d}t} = \frac{\mathrm{i}}{\hbar}\left[\hat{H}_{\mathrm{LC}}, \hat{Q}\right] = \omega_c Q_{\mathrm{zpf}}\left(c^\dagger + \hat{c}\right)\,, \tag{G4}$$

where $\hat{Q} = \mathrm{i}Q_{\mathrm{zpf}}\left(\hat{c}^\dagger - \hat{c}\right)$ with $Q_{\mathrm{zpf}} = \sqrt{\hbar C \omega_c/2}$ and C is capacity. The magnetic part is quantized via

$$\delta\hat{\mathbf{m}}(\mathbf{r}, t) = \delta\mathbf{m}(\mathbf{r})\,\mathrm{e}^{-\mathrm{i}\omega_m t}\hat{m} + h.c.\,, \tag{G5}$$

where we consider a splitting of the reduced magnetization, $\mathbf{M}/\mathbf{M}_s$ with $\mathbf{M}_S$ being the saturation magnetization, into a static magnetic ground-state plus the dynamic part on top, $\mathbf{m}(\mathbf{r}, t) = \mathbf{m}_0(\mathbf{r}) + \delta\mathbf{m}(\mathbf{r}, t)$. Inserting these expressions into equation (G2) one obtains

$$\hat{H}_{\mathrm{Zeeman}} = \frac{\mu_0 \omega_c Q_{\mathrm{zpf}}}{4\pi}\left(\hat{c}^\dagger + \hat{c}\right)\left[\hat{m}^\dagger \int \mathrm{d}r^3\, \delta\mathbf{m}(\mathbf{r}) \int_U \frac{I[dl \times \mathbf{r}']}{|\mathbf{r}'|^3} + h.c.\right]\,, \tag{G6}$$

which can be used to estimate the coupling strength of the resonant interaction between magnons and microwave photons described by the process $\hat{m}^\dagger\hat{c} + h.c.$

G.2. Photoelastic Interaction

Following the model described in [113], we extend the analysis from a 2D waveguide picture to 3D resonators by integrating over all spatial dimensions instead of only over a resonator cross-section. There is a formal caveat in making this transition: the system modes $\psi_n = \begin{pmatrix} \boldsymbol{E}_n & \boldsymbol{H}_n \end{pmatrix}^T$ (where $\boldsymbol{E}_n$ and $\boldsymbol{H}_n$ are the electric and magnetic field distributions of the mode) are quasi-normal modes, such that the strict assumptions in [113] become approximate. In this framework, the general solution is a decomposition $\psi = \sum_n a_n \psi_n$, and the classical equations of motion for the complex amplitudes a_n for the simplest magnetoelastic interactions take the form

$$(\partial_t + \Gamma_n)\, a_n = \frac{\mathrm{i}}{\mathcal{E}_n} \sum_m \left[\mathrm{e}^{-\mathrm{i}\Omega_{\mathrm{mech}} t} \omega_m Q_{nm} b + \mathrm{c.c.} \right] a_m \,, \tag{G7}$$

where b is the mechanical mode complex amplitude, ω_n and Ω_{mech} are the optical and mechanical mode frequencies, $\Gamma_n = \langle n | \mathrm{diag}(\sigma, 0) | n \rangle$ is the matrix element corresponding to intrinsic Joule heating losses for a material with conductivity σ, $\mathcal{E}_n = \langle n | \mathrm{diag}(\epsilon' \varepsilon_0, \mu\mu_0) | n \rangle$ is the mode energy normalization, and the elements Q_{nm} describe the strength of the coupling.

The nature of the interaction dictates that the lowest-order terms remaining in the expansion give the classical photon-pressure interaction part of the Hamiltonian presented in equation (1). Comparing equation (G7) to the Heisenberg equation $\mathrm{d}\hat{a}_n/\mathrm{d}t = \mathrm{i}/\hbar \left[\hat{H}, \hat{a}_n\right]$, one can immediately find the relation between the sought coupling constant and the matrix elements described above:

$$g_{ab}^{(nm)} = \frac{\omega_m Q_{nm}}{\mathcal{E}_n} \,. \tag{G8}$$

In our geometry, the interaction elements Q_{nm} are primarily determined by two mechanisms. The first mechanism is photoelasticity–changes in the material permittivity due to deformation, $\Delta\varepsilon_{ij} = -\varepsilon_r^2 p_{ijkl} \epsilon_{kl}$, where p_{ijkl} is the photoelastic tensor and ε_r is the real part of the permittivity. This interaction produces a matrix element

$$Q_{nm}^{(\mathrm{PE})} = \varepsilon_0 \varepsilon_r^2 \int_V d^3 r \sum_{ijkl} E_i^{(n)*} E_j^{(m)} p_{ijkl} \epsilon_{kl} \,. \tag{G9}$$

The second mechanism is coupling due to boundary motion, which can be understood as arising from changes in optical mode frequencies due to deformation of the nanoresonator. This effect can be calculated perturbatively (see [114]) using the following expression:

$$\begin{aligned} Q_{nm}^{(\mathrm{MB})} = \int_\Gamma d^2 r \, (\boldsymbol{u}^* \cdot \hat{\boldsymbol{n}}) \Big[(\varepsilon_a - \varepsilon_b) \varepsilon_0 \left(\hat{\boldsymbol{n}} \times \boldsymbol{e}^{(n)} \right)^* \cdot \left(\hat{\boldsymbol{n}} \times \boldsymbol{e}^{(m)} \right) + \\ \left(\varepsilon_b^{-1} - \varepsilon_a^{-1} \right) \left(\hat{\boldsymbol{n}} \cdot \boldsymbol{d}^{(n)} \right)^* \left(\hat{\boldsymbol{n}} \cdot \boldsymbol{d}^{(m)} \right) \Big] \,, \end{aligned} \tag{G10}$$

or alternatively evaluated directly by recomputing the optical modes in the deformed geometry.

G.3. Numeric mode calculations

In the course of calculating the interaction strengths we also need to know the mode distributions of the confined magnetic $\delta\boldsymbol{m}$, mechanical $\boldsymbol{u}$ and optical $\{\boldsymbol{E}, \boldsymbol{H}\}$ modes of the sample. We are using the axial symmetry of the system to simplify individual eigenproblems by considering an axial number $n_\varphi = 0$, mainly limited by the coupling to microwave resonator—the microwave wavelength is much larger than structure's size so that coupling to modes with $n_\varphi > 0$ is greatly suppressed.

We use a custom proprietary finite-elements solver provided by partners at CEA for solving magnetic and elastic eigenproblems, for example in [100]. The mechanical problem is solved using the linear isotropic elasticity equations [115] using Young's modulus $E = 198\,\mathrm{Gpa}$, Poisson ratio $\nu = 0.3$ and density $\rho = 5170\ \mathrm{kg\,m^{-3}}$. Magnetic eigenmodes are similarly calculated for the Landau Lifshitz Gilbert equation [116] linearized around the equilibrium vortex-state magnetization $\boldsymbol{m}_0$; the parameters for magnetic calculations are $A_{ex} = 3.7\ \mathrm{pJ\,m^{-1}}$, $M_s = 139\ \mathrm{kA\,m^{-1}}$, and anisotropy is ignored.

For the optical quasi-normal (including radiation and material losses for our open resonator) mode calculation we implement the weak form described in [117] modified by also including a perfectly match layer boundary to make the radiation losses calculation more accurate. Optically YIG has a transparency window in the near infrared extending all the way to the telecom c-band, although peak transparency is at higher wavelength [118]. Within the band the refractive index is taken to be $n \approx 2.19$, at the lower end for typical optical microresonator materials. For estimating intrinsic losses we take $\epsilon'' = 4 \times 10^{-3}$.

We neglect the optical dispersion (wavelength dependence) in the YIG for simplicity. The custom FENICs solver is set up for the C_1 continuous $\boldsymbol{H}$-field with mixed elements, Nédélec for H_r, H_z components of field and Lagrange for the azimuthal component H_φ to improve the solver's convergence.

ORCID iDs

F Engelhardt 0000-0002-4225-9518
A V Bondarenko 0000-0002-9092-093X
S Viola Kusminskiy 0000-0002-6373-7478
V A S V Bittencourt 0000-0002-0701-7142

References

[1] Yin J *et al* 2020 *Nature* **582** 501
[2] Ekert A K 1991 *Phys. Rev. Lett.* **67** 661
[3] Bennett C H, Brassard G and Mermin N D 1992 *Phys. Rev. Lett.* **68** 557
[4] Tittel W, Brendel J, Zbinden H and Gisin N 2000 *Phys. Rev. Lett.* **84** 4737
[5] Bennett C H 1992 *Phys. Rev. Lett.* **68** 3121
[6] Bennett C H, Brassard G, Crépeau C, Jozsa R, Peres A and Wootters W K 1993 *Phys. Rev. Lett.* **70** 1895
[7] Furusawa A, Sørensen J L, Braunstein S L, Fuchs C A, Kimble H J and Polzik E S 1998 *Science* **282** 706
[8] Boschi D, Branca S, De Martini F, Hardy L and Popescu S 1998 *Phys. Rev. Lett.* **80** 1121
[9] Vaidman L 1994 *Phys. Rev. A* **49** 1473
[10] Braunstein S L and Kimble H J 1998 *Phys. Rev. Lett.* **80** 869
[11] Bouwmeester D, Pan J-W, Mattle K, Eibl M, Weinfurter H and Zeilinger A 1997 *Nature* **390** 575
[12] Riebe M *et al* 2004 *Nature* **429** 734
[13] Barrett M D *et al* 2004 *Nature* **429** 737
[14] van Loock P and Braunstein S L 2000 *Phys. Rev. Lett.* **84** 3482
[15] Jiang L, Taylor J M, Sørensen A S and Lukin M D 2007 *Phys. Rev. A* **76** 062323
[16] Pirandola S and Braunstein S L 2016 *Nature* **532** 169
[17] Zhuang Q, Zhang Z and Shapiro J H 2018 *Phys. Rev. A* **97** 032329
[18] Guo X, Breum C R, Borregaard J, Izumi S, Larsen M V, Gehring T, Christandl M, Neergaard-Nielsen J S and Andersen U L 2020 *Nat. Phys.* **16** 281
[19] Zhang Z, Mouradian S, Wong F N C and Shapiro J H 2015 *Phys. Rev. Lett.* **114** 110506
[20] Xia Y, Agrawal A R, Pluchar C M, Brady A J, Liu Z, Zhuang Q, Wilson D J and Zhang Z 2023 *Nat. Photon.* **17** 470
[21] Cirac J I, Zoller P, Kimble H J and Mabuchi H 1997 *Phys. Rev. Lett.* **78** 3221
[22] Acín A, Cirac J I and Lewenstein M 2007 *Nat. Phys.* **3** 256
[23] Caleffi M, d'Avossa L, Han X and Sara Cacciapuoti A 2026 *IEEE Commun. Surveys Tutorials* **28** 4195
[24] Arute F *et al* 2019 *Nature* **574** 505
[25] Magnard P *et al* 2020 *Phys. Rev. Lett.* **125** 260502
[26] Lauk N, Sinclair N, Barzanjeh S, Covey J P, Saffman M, Spiropulu M and Simon C 2020 *Quantum Sci. Technol.* **5** 020501
[27] Rueda A, Hease W, Barzanjeh S and Fink J M 2019 *npj Quantum Inf.* **5** 108
[28] Zhang F-Y and Yang C-P 2021 *Quantum Sci. Technol.* **6** 025003
[29] Tsang M 2011 *Phys. Rev. A* **84** 043845
[30] d'Avossa L, Caleffi M, Wang C, Illiano J, Zorzetti S and Cacciapuoti A S 2023 *2023 IEEE Int. Conf. on Quantum Computing and Engineering (QCE)* vol 01 pp 1325–34
[31] Sahu R, Qiu L, Hease W, Arnold G, Minoguchi Y, Rabl P and Fink J M 2023 *Science* **380** 718
[32] Andrews R W, Peterson R W, Purdy T P, Cicak K, Simmonds R W, Regal C A and Lehnert K W 2014 *Nat. Phys.* **10** 321
[33] Miao Q and Wu D 2024 *Sensors* **24** 7712
[34] Ren Y-l 2022 *Opt. Lett.* **47** 1125
[35] Shang X, Chen D-D, Xie H, Lin G-W and Lin X-M 2024 *Phys. Lett. A* **493** 129263
[36] Zheng Q, Zhong W, Cheng G and Chen A 2024 *J. Appl. Phys.* **135** 084401
[37] Jia J, Huang J, Zhang F and Zhang M 2025 *Sci. Rep.* **15** 11606
[38] Meesala S, Lake D, Wood S, Chiappina P, Zhong C, Beyer A D, Shaw M D, Jiang L and Painter O 2024 *Phys. Rev. X* **14** 031055
[39] Zhong C, Han X, Tang H X and Jiang L 2020 *Phys. Rev. A* **101** 032345
[40] Zhong C *et al* 2020 *Phys. Rev. Lett.* **124** 010511
[41] Zhong C, Han X and Jiang L 2022 *Phys. Rev. Appl.* **18** 054061
[42] Zhong C, Li F, Meesala S, Wood S, Lake D, Painter O and Jiang L 2024 *Phys. Rev. Appl.* **22** 064047
[43] Wei T, Wu D, Miao Q, Yang C and Luo J 2022 *Opt. Express* **30** 10135
[44] Rau C L, Kyle A, Kwiatkowski A, Shojaee E, Teufel J D, Lehnert K W and Dennis T 2022 *Phys. Rev. Appl.* **17** 044057
[45] Li J, Zhu S-Y and Agarwal G S 2018 *Phys. Rev. Lett.* **121** 203601
[46] Chumak A V, Vasyuchka V I, Serga A A and Hillebrands B 2015 *Nat. Phys.* **11** 453
[47] Chumak A V *et al* 2022 *IEEE Trans. Magn.* **58** 1
[48] Lachance-Quirion D, Tabuchi Y, Gloppe A, Usami K and Nakamura Y 2019 *Appl. Phys. Express* **12** 070101
[49] Flebus B *et al* 2024 *J. Phys.: Condens. Matter* **36** 363501
[50] Hisatomi R, Osada A, Tabuchi Y, Ishikawa T, Noguchi A, Yamazaki R, Usami K and Nakamura Y 2016 *Phys. Rev. B* **93** 174427
[51] Xie J-k, Ma S-l and Li F-l 2020 *Phys. Rev. A* **101** 042331
[52] Cai Q, Liao J, Shen B, Guo G and Zhou Q 2021 *Phys. Rev. A* **103** 052419
[53] Ren Y-l, Ma S-l, Xie J-k, Li X-k, Cao M-t and Li F-l 2022 *Phys. Rev. A* **105** 013711

[54] Ren Y-l, Xie J-k, Li X-k, Ma S-l and Li F-l 2022 *Phys. Rev. B* **105** 094422
[55] Xie J, Ma S, Ren Y, Li X, Gao S and Li F 2023 *New J. Phys.* **25** 073009
[56] Wang Y-D, Chesi S and Clerk A A 2015 *Phys. Rev. A* **91** 013807
[57] An K *et al* 2020 *Phys. Rev. B* **101** 060407
[58] Müller M *et al* 2024 *Phys. Rev. B* **109** 024430
[59] Engelhardt F, Bittencourt V, Huebl H, Klein O and Kusminskiy S V 2022 *Phys. Rev. Appl.* **18** 044059
[60] Müller M, Weber J, Goennenwein S, Kusminskiy S V, Gross R, Althammer M and Huebl H 2024 *Phys. Rev. Appl.* **21** 034032
[61] Ba Y, Puebla J, Yamamoto K, Hwang Y, Liao L, Maekawa S, Klein O and Otani Y 2025 *Phys. Rev. B* **111** 104401
[62] Rashedi A, Ebrahimi M, Huang Y, Rudd M, Davis J and Bittencourt V 2025 *Phys. Rev. Appl.* **24** 054017
[63] Hatanaka D, Asano M, Kurosu M, Taniyasu Y, Okamoto H and Yamaguchi H 2025 *Phys. Rev. Appl.* **24** 064053
[64] Adesso G and Illuminati F 2005 *Phys. Rev. Lett.* **95** 150503
[65] Heyroth F, Hauser C, Trempler P, Geyer P, Syrowatka F, Dreyer R, Ebbinghaus S, Woltersdorf G and Schmidt G 2019 *Phys. Rev. Appl.* **12** 054031
[66] Merbouche H *et al* 2024 *Phys. Rev. Appl.* **21** 064041
[67] Ngouagnia Yemeli I *et al* 2025 *Phys. Rev. Lett.* **135** 056703
[68] Soares G *et al* 2026 Nonlinear mode interactions under parametric excitation in a YIG microdisk (arXiv:2601.05775 [cond-mat.mes-hall])
[69] Yambe T, Taniguchi K, Kitai T, Sato D, Gao S, Kumazaki H, Fujii S, Tanabe T, Iwamoto S, and Ota Y 2026 High-Q Magneto-optical microdisk resonators based on monocrystalline bismuth-substituted Yttrium iron garnets (arXiv:2609.22841 [physics.optics])
[70] Pacewicz A, Krupka J, Pullar R C, Bogorodzki P and Salski B 2027 *Mater. Res. Bull.* **205** 114409
[71] Mallmann E J J, Sombra A S B, Goes J C and Fechine P B A 2013 *Solid State Phenomena* **202** 65
[72] Klingler S, Maier-Flaig H, Dubs C, Surzhenko O, Gross R, Huebl H, Goennenwein S T B and Weiler M 2017 *Appl. Phys. Lett.* **110** 092409
[73] Maier-Flaig H, Klingler S, Dubs C, Surzhenko O, Gross R, Weiler M, Huebl H and Goennenwein S T B 2017 *Phys. Rev. B* **95** 214423
[74] Kosen S, van Loo A F, Bozhko D A, Mihalceanu L and Karenowska A D 2019 *APL Mater.* **7** 101120
[75] Adesso G, Serafini A and Illuminati F 2004 *Phys. Rev. Lett.* **93** 220504
[76] Aspelmeyer M, Kippenberg T J and Marquardt F 2014 *Rev. Mod. Phys.* **86** 1391
[77] Spencer E G and LeCraw R C 1958 *Phys. Rev. Lett.* **1** 241
[78] Brown W F 1966 *Magnetoelastic Interactions* (*Springer Tracts in Natural Philosophy*) vol 9 (Springer)
[79] Fan Z-Y, Qiu L, Gröblacher S and Li J 2023 *Laser Photon. Rev.* **17** 2200866
[80] Liu M-Y, Gong Y, Chen J, Wang Y-W and Xiong W 2025 *Chin. Phys. B* **34** 057202
[81] Huebl H, Zollitsch C W, Lotze J, Hocke F, Greifenstein M, Marx A, Gross R and Goennenwein S T B 2013 *Phys. Rev. Lett.* **111** 127003
[82] Potts C A and Davis J P 2020 *Appl. Phys. Lett.* **116** 263503
[83] Zare Rameshti B, Viola Kusminskiy S, Haigh J A, Usami K, Lachance-Quirion D, Nakamura Y, Hu C-M, Tang H X, Bauer G E W and Blanter Y M 2022 *Phys. Rep.* **979** 1
[84] Li B-B, Ou L, Lei Y and Liu Y-C 2021 *Nanophotonics* **10** 2799
[85] Walls D F and Milburn G J 2025 *Quantum Optics* (Graduate Texts in Physics) (Springer)
[86] Simon R 2000 *Phys. Rev. Lett.* **84** 2726
[87] Duan L-M, Giedke G, Cirac J I and Zoller P 2000 *Phys. Rev. Lett.* **84** 2722
[88] Peres A 1996 *Phys. Rev. Lett.* **77** 1413
[89] Horodecki P 1997 *Phys. Lett. A* **232** 333
[90] Vidal G and Werner R F 2002 *Phys. Rev. A* **65** 032314
[91] Wiseman H M and Milburn G J 2009 *Quantum Measurement and Control* (Cambridge University Press)
[92] Scully M O and Zubairy M S 1997 *Quantum Optics* (Cambridge University Press)
[93] Graf J, Sharma S, Huebl H and Kusminskiy S V 2021 *Phys. Rev. Res.* **3** 013277
[94] Demirchyan S S, Krichevsky D M and Belotelov V I 2026 *J. Appl. Phys.* **139** 113903
[95] Liu T, Zhang X, Tang H X and Flatté M E 2016 *Phys. Rev. B* **94** 060405(R)
[96] Viola Kusminskiy S, Tang H X and Marquardt F 2016 *Phys. Rev. A* **94** 033821
[97] Streltsov A, Adesso G and Plenio M B 2017 *Rev. Mod. Phys.* **89** 041003
[98] Wang Y-D and Clerk A A 2012 *New J. Phys.* **14** 105010
[99] Ferraro A, Olivares S and Paris M G A 2005 Gaussian states in continuous variable quantum information (arXiv:quant-ph/0503237)
[100] Bondarenko A V, Engelhardt F, Kounalakis M, Valet T, Klein O, Bauer G E W, Kusminskiy S V and Blanter Y M 2026 Magnetoelastic conversion in integrated YIG nanostructures (arXiv:2602.20458 [cond-mat])
[101] Graf J, Pfeifer H, Marquardt F and Viola Kusminskiy S 2018 *Phys. Rev. B* **98** 241406(R)
[102] Haigh J, Chakalov R and Ramsay A 2020 *Phys. Rev. Appl.* **14** 044005
[103] Zhu N, Zhang X, Han X, Zou C-L, Zhong C, Wang C-H, Jiang L and Tang H X 2020 *Optica* **7** 1291
[104] Booth R C and White E A D 1984 *J. Phys. D: Appl. Phys.* **17** 579
[105] Vojna D, Slezák O, Lucianetti A and Mocek T 2019 *Appl. Sci.* **9** 3160
[106] Anetsberger G, Rivière R, Schliesser A, Arcizet O and Kippenberg T J 2008 *Nat. Photon.* **2** 627
[107] Nguyen D T, Baker C, Hease W, Sejil S, Senellart P, Lemaître A, Ducci S, Leo G and Favero I 2013 *Appl. Phys. Lett.* **103** 241112
[108] Sun Z, Withington S, Thomas C N and Zhao S 2025 *Supercond. Sci. Technol.* **38** 095012
[109] Valet T, Yamamoto K, Pigeau B, de Loubens G and Klein O 2025 Field theory of linear spin-waves in finite textured ferromagnets (arXiv:2503.06557 [cond-mat])
[110] Valet T, Yamamoto K, Pigeau B, de Loubens G and Klein O 2025 The orbital angular momentum of Azimuthal spin-waves (arXiv:2503.06556 [cond-mat])
[111] Qiu L, Shomroni I, Seidler P and Kippenberg T J 2020 *Phys. Rev. Lett.* **124** 173601
[112] Kogias I, Lee A R, Ragy S and Adesso G 2015 *Phys. Rev. Lett.* **114** 060403

[113] Wolff C, Smith M J A, Stiller B and Poulton C G 2021 *JOSA B* **38** 1243
[114] Johnson S G, Ibanescu M, Skorobogatiy M A, Weisberg O, Joannopoulos J D and Fink Y 2002 *Phys. Rev. E* **65** 066611
[115] Landau L D, Kosevich A M, Lifshitz E M and Pitaevskii L P 1986 *Theory of Elasticity: Volume 7* (Elsevier)
[116] Brown W F 1963 *Micromagnetics* (Interscience Publishers)
[117] Grudinin I S and Yu N 2012 *JOSA B* **29** 3010
[118] Dillon J 1959 *J. Phys. Radium* **20** 374